

# STARS

University of Central Florida  
**STARS**

---

Electronic Theses and Dissertations, 2004-2019

---

2012

## Random Transformations Of Optical Fields And Applications

Thomas Kohlgraf-Owens  
*University of Central Florida*



Part of the [Electromagnetics and Photonics Commons](#), and the [Optics Commons](#)

Find similar works at: <https://stars.library.ucf.edu/etd>

University of Central Florida Libraries <http://library.ucf.edu>

This Doctoral Dissertation (Open Access) is brought to you for free and open access by STARS. It has been accepted for inclusion in Electronic Theses and Dissertations, 2004-2019 by an authorized administrator of STARS. For more information, please contact [STARS@ucf.edu](mailto:STARS@ucf.edu).

---

### STARS Citation

Kohlgraf-Owens, Thomas, "Random Transformations Of Optical Fields And Applications" (2012).  
*Electronic Theses and Dissertations, 2004-2019*. 2346.  
<https://stars.library.ucf.edu/etd/2346>



# RANDOM TRANSFORMATIONS OF OPTICAL FIELDS AND APPLICATIONS

by

THOMAS W. KOHLGRAF-OWENS  
B.S. University of Alabama in Huntsville, 2005  
M.S. University of Central Florida, 2007

A dissertation submitted in partial fulfillment of the requirements  
for the degree of Doctor of Philosophy  
in the College of Optics and Photonics  
at the University of Central Florida  
Orlando, Florida

Fall Term  
2012

Major Professor: Aristide Dogariu

© 2012 Thomas Kohlgraf-Owens

## **ABSTRACT**

The interaction of optical waves with material systems often results in complex, seemingly random fields. Because the fluctuations of such fields are typically difficult to analyze, they are regarded as noise to be suppressed. Nevertheless, in many cases the fluctuations of the field result from a linear and deterministic, albeit complicated, interaction between the optical field and the scattering system. As a result, linear systems theory (LST) can be used to frame the scattering problem and highlight situations in which useful information can be extracted from the fluctuations of the scattered field.

Three fundamental problems can be posed in LST regardless of the nature of the system: one direct and two inverse problems. The direct problem attempts to predict the response of a known system to a known input. The problem may be simple enough to admit analytical solutions as in the case of homogeneous materials, phase and amplitude screens, and weakly scattering materials; or the problem may require the use of numerical techniques.

This dissertation will focus on the two inverse problems, namely the determination of either the excitation field or the scattering system. Traditionally, the excitation determination problem has relied on designing optical systems that respond to the property of interest in a simple, easily quantified way. For example, gratings can be used to map wavelength onto direction of propagation while waveplates and polarizers can map polarization properties onto intensity. The primary difficulty with directly applying the concepts of LST to scattering systems

is that, while the outputs are still combinations of the inputs, they are not "simple" combinations such as Fourier transforms or spatially dispersed spectral components of the input spectrum. Instead, the scattered field can be thought of as a massive sampling and mixing of the excitation field. This dissertation will show that such complicated sampling functions can be characterized and that the corresponding scattering medium can then be used as an optical device such as a lens, polarimeter, or spectrometer.

The second inverse problem, system determination, is often more difficult because the problem itself may be ill-posed. For scattering systems that are dominated by low-order scattering, the statistical properties of the scattered light may serve as a fingerprint for material discrimination; however, in many situations, the statistical properties of the output do not depend on the material properties. Rather than analyzing the scattered field from one realization of the random interaction, several measurement techniques have been developed that attempt to extract information about the material system from modifications of the scattered field in response to changes in either the excitation or the intrinsic dynamics of the medium itself. One such technique is dynamic light scattering. This dissertation includes an extension to this method that allows for a polarimetric measurement of the scattered light using a reference beam with controllable polarization. Another system determination problem relates to imaging the reflectivity of a target that is being randomly illuminated. It will be demonstrated that an approach based on the correlation between the integrated scattered intensity and the corresponding illumination intensity distribution can prove superior to standard imaging microscopy.

To my wife, Dana, and my son, Andrew.

## **ACKNOWLEDGMENTS**

I would like to thank my advisor, Dr. Aristide Dogariu, both for his continuous support during my graduate career and for an untold number of discussions over a wide range of topics.

I appreciate the time and participation of my committee members.

I am grateful to the Photonic Diagnostics of Random Media group for all of their support and beneficial discussions during my research. I am especially indebted to Dr. Jeremy Ellis, from whom I learned a great amount about polarization and coherence.

Finally, I would like to thank my family for their support and encouragement over the years; especially my wife, Dana. Andrew, you have been source of continuous joy since you were born.

## TABLE OF CONTENTS

LIST OF FIGURES .....	ix
LIST OF TABLES .....	xii
CHAPTER 1: INTRODUCTION .....	1
CHAPTER 2: STATISTICS OF RANDOM FIELDS .....	6
CHAPTER 3: MEDIA CHARACTERIZATION .....	14
3.1 Statistics of Transfer Matrices .....	15
3.2 Global Transfer Matrix Dynamics .....	20
3.2.1 Dynamic Light Scattering And Diffusive Wave Spectroscopy .....	20
3.2.2 Fluctuation Polarimetry .....	24
3.3 Local Transfer Matrix Dynamics.....	34
3.3.1 Digital Speckle Photography And Digital Speckle Interferometry .....	34
3.3.2 Correlation Imaging .....	39
CHAPTER 4: OUTPUT FIELD MANIPULATION .....	55
4.1 Searching for Transfer Matrices .....	55
4.2 Measuring Transfer Matrices.....	61
CHAPTER 5: INPUT FIELD CHARACTERIZATION USING MEASURED TRANSFER MATRICES .....	64
5.1 Polarimetry .....	64
5.2 Spectroscopy.....	72



CHAPTER 6: SUMMARY OF ORIGINAL CONTRIBUTIONS AND CONCLUSIONS.....	75
APPENDIX: PUBLICATIONS AND PRESENTATIONS.....	81
A. Refereed Papers .....	82
B. Oral Presentations .....	83
C. Posters .....	84
LIST OF REFERENCES .....	85

## LIST OF FIGURES

Figure 3.1: Illumination and detection set-up for measuring scattering from asphalt samples..	17
Figure 3.2: Spread of polarization states after scattering from asphalt. -Q polarized light was incident on the sample. ....	18
Figure 3.3: (a) The scattered field in DLS is composed of single scattering contributions from many particles. (b) The scattered field in DWS is due to diffusive, multiple scattering. ....	20
Figure 3.4: The set-up used to test the fluctuation polarimetry theory. The abbreviations are ND for neutral density filter, Pol for polarizer, QWP for quarter waveplate, and HWP for half waveplate.....	31
Figure 3.5. The experimental (red dots) and theoretical (blue line) intensity contrasts for (a) vertically polarized, (b) partially vertically polarized with $D \approx 0.455$ , (c) elliptically polarized, and (d) unpolarized fluctuating fields as a function of the orientation of a linearly polarized reference field. All of the plots are on the same scale. The DOP and Stokes vector for the best fit to the experimental contrasts are indicated for each plot.....	33
Figure 3.6: Basic set-up to perform speckle photography. A surface is coherently illuminated by a point source or laser. The speckle pattern at the surface is imaged onto a detector array by a lens system.....	34
Figure 3.7: Cross-correlating sections of two speckle fields gives the local shift of the speckle patterns. The local shifts can be used to generate a flow map of the surface to visualize the local in-plane shifts.....	36
Figure 3.8: Basic set-up to perform speckle interferometry. A surface is coherently illuminated by a point source or laser. The speckle pattern generated by the surface is interfered with a reference beam or a speckle pattern generated by a reference surface. The speckle pattern at the surface is imaged onto a detector array by a lens system. ....	37
Figure 3.9: Experimental geometry for measuring in plane surface displacements. The test surface is illuminated by two plane waves at an equal angle $\theta$ from the average surface normal.....	38
Figure 3.10: Steps taken in the numerical experiment to compare CI with traditional, spatially-resolved CCD based imaging. ....	43

Figure 3.11: Single realizations of the random illumination patterns for (a) fully developed speckle pattern, (b) and (c) Gaussian spots covering 20% and 1% of the illuminated area, respectively. (d) Target consisting of five stripes with reflectivities of 0.2, 0.4, 0.6, 0.8, and 1. The single stripe targets used stripes of the same dimensions located at the position of the top stripe in (d)...... 45

Figure 3.12: (a) “Blurred” CCD image and (b) correlation image of a stripe with  $R=1$ , illuminated with 10,000 realizations of the 1% coverage illumination having one photon per spot on average. The total number of photons reflected towards the detectors is 292..... 50

Figure 3.13: (a) “Blurred” CCD image and (b) correlation image of a stripe with  $R=0.2$ , illuminated with 10,000 realizations of the 1% coverage illumination having one photon per spot on average. The total number of photons reflected towards the detectors is 49..... 50

Figure 3.14: Plot of the mean value for each stripe as seen in the CCD and CI images for the three illumination conditions, normalized to the mean for the  $R = 1$  stripe, when (a) the total number of photons in the image and (b) the number of photons per speckle are constant. In (a) the CCD output changes very similarly under the three illumination conditions, but CI result becomes nonlinear as the number of speckles per pattern decreases. In (b), the correlation changes similarly for each type of illumination, but the CCD, while still linear, varies depending on the total photon flux because of the fixed level of the read noise. The lines only serve as guides..... 52

Figure 3.15: Schematic of a CI microscope. The SLM is used to create a spatially varying polarization state on the laser beam, and a polarizer is used to turn the polarization into a spatially varying intensity pattern. The intensity pattern is projected onto a sample through a microscope objective, and the reflected light is either imaged onto a CCD or integrated on a photodiode..... 53

Figure 3.16: (a) Correlation image and (b) standard CCD image taken of a microscope calibration target. The stripes are approximately  $2\mu\text{m}$  wide and spaced by  $10\mu\text{m}$ . The size of the illumination spots in the target plane are approximately  $2\mu\text{m}$ ...... 54

Figure 4.1: An output can be chosen by varying the input field and having a detector report the output. A blind search where the feedback is only used to determine if the desired output has been produced could take a significant amount of time to complete, but if the feedback is used intelligently, the search time can be decreased dramatically. .... 56

Figure 4.2: Bases of focusing via random media. (a) Scalar field in the output plane is the result of contributions from each input point. The phase of each contribution can be controlled to maximize the resulting summation as indicated in green. (b) Field after manipulating the incident wavefront..... 57

Figure 4.3: Set-up for controlling the field generated by scattering from a random medium. ....	59
Figure 4.4: An array of transmitters and an array of receivers separated by a homogeneous material (a) or a randomly scattering material (b). In the homogeneous case, the transmitters are able to focus their power onto the receivers, but the scattering medium dissipates their power. ....	62
Figure 4.5: (a) An antenna sends a pulse through a scattering medium while other antennas record the scattered field. (b) The recording antennas send the phase conjugate of the previously recorded pulse back through the medium. After propagating through the medium, the signal focuses onto the original antenna. ....	63
Figure 5.1: Light scattering inside a random slab. ....	66
Figure 5.2: Geometry of a spatially resolved TM based polarimeter. A thin layer of scattering material is applied to the face of an imaging fiber bundle to allow access to local states of polarization. ....	69
Figure 5.3: Example data collected with TM based polarimetry concept. ....	69
Figure 5.4: The U component of the Stokes vector for a checker pattern generated by a SLM. (a)The measurement made by the fiber polarimeter. (b)The measurement made using a polarizer and CCD array. The white box indicates the approximate area measured by the fiber polarimeter. ....	71
Figure 5.5: Polarimetric data processed using groups of 4, 8, 24, and 40 speckles per polarimeter. ....	72
Figure 5.6: Some example spectra measured using a conventional spectrometer (red line) and a random material (blue line). ....	73
Figure 5.7: An example of a spatially varying spectrum measured using a random material. ....	74

## LIST OF TABLES

Table 3.1: Polarimetric properties of different asphalt samples.....	19
Table 3.2: Visibility and contrast when a single stripe target is imaged using CI and a conventional CCD with a constant number of photons per illumination pattern. R is the stripe's reflectivity, and N is the number of photons reflected from the stripe. CCD is calculated from the spatially resolved detection of the reflected photons, and Blurred is from the same image but with the Gaussian blur kernel applied as described in the text. The results in the "CCD" and "Blurred" columns represent the average for the three types of illumination. The remaining columns contain the results corresponding to the bucket detectors. "Ideal" indicates an ideal photon counter while "SPAD" denotes the single photon avalanche photodiode. In the CI case, the performance depends on the illumination. "Speckle", "20%", and "1%" correspond to the three types of illumination discussed in text: fully developed speckle patterns and the Gaussian spots with 20% and 1% coverage, respectively. ....	48
Table 3.3: Visibility for imaging the single stripe targets with an average of one photon per illumination spot. The meaning of the headings is the same as in Table 3.2.....	49
Table 3.4: Visibility parameter when the random illumination has 20% coverage and an average of one photon per spot. The number of stripes in the target is either 1 or 5 as indicated. ....	51

## CHAPTER 1: INTRODUCTION

Classical electrodynamics regards light as a fluctuating electromagnetic field subject to Maxwell's equations. This interpretation leads to a wave equation that describes the propagation of the light through both free space and some material systems. Naturally, once we have described the field propagation, we can also describe the evolution of other properties of light such as intensity, polarization, and coherence. Often, we discuss the results of propagation as a transfer from one spatial location to another. The essential idea of a transfer function is that the input to the system is deterministically mapped onto the output of the system, though the mapping may vary spatially, temporally, and spectrally. For traditional optical systems using lenses, gratings, and so on, the view of transfer functions has found wide application through Fourier optics, but it is of less apparent use for scattering systems [1].

The general case of the transfer through a linear medium can be written as

$$\vec{E}_{out}(\mathbf{r}, \omega, t) = \int_{-\infty}^t \int_{-\infty}^{\infty} \overline{\overline{T}}(\mathbf{r}, \mathbf{r}', \omega, t') \vec{E}_{in}(\mathbf{r}', \omega, t') d\mathbf{r}' dt' \quad (1.1)$$

where  $\overline{\overline{T}}$  is a matrix of transfer functions that take a field at a given time  $t'$ , location  $\mathbf{r}'$ , and frequency  $\omega$  and map it onto another field at a later time  $t$ , location  $\mathbf{r}$ , and the same frequency. We will refer to the collection of measured transfer functions,  $\overline{\overline{T}}$ , as the transmission matrix (TM) of the material. Systems that can be described by Equation 1.1 form the basis for linear systems theory (LST).

For simple systems, analytical formulas may be used to describe the transformation  $\overline{\overline{T}}$ . A lens serves as a good example; Fourier optics allows the propagation of a field from any plane before the lens to any plane after the lens to be described quite simply. In effect, each combination of input plane, output plane, and lens focal length is a different system; however, a single expression describes all of the possible combinations. Analytical descriptions of the transmission through random systems do not exist in many cases. The transmission is still deterministic for a single realization of the randomness, but the transmission function must either be calculated for the exact configuration of the medium or directly measured because it depends on the properties of the input in a complicated, seemingly random way.

Three fundamental problems can be posed in LST regardless of the nature of the system, one direct problem and two inverse problems. The direct problem attempts to predict the response of a known system to a known input. The problem may be simple enough to admit analytical solutions as in the case of homogeneous materials, phase and amplitude screens, and weakly scattering materials, or the problem may require numerical techniques to find a solution for the particular system. There are, of course, many different techniques and levels of approximation that have been developed and applied to the direct problem depending on which property of the output is of interest. A sort of corollary to the direct problem is that if the input to the linear system can be controlled specific outputs can be selected. In the context of optics, recent experiments have demonstrated focusing light through strongly scattering media as one application of the forward problem [2,3].

The formulation of inverse problems refer to finding either the excitation field or the

scattering system. Traditionally, the excitation determination problem has relied on designing optical systems that respond to the property of interest in a simple, easily quantified way. For example, gratings can be used to map wavelength onto direction of propagation, and waveplates and polarizers map polarimetric properties onto intensity. The primary difficulty with directly applying the concepts of TM to scattering systems is that, while the outputs are still combinations of the inputs, they are not "simple" combinations such as Fourier transforms or spatially dispersed spectral components of the input spectrum. In one of the most commonly considered scattering situations, the Gaussian scattering regime, it is relatively easy to show that the statistical properties of the scattered field depend only on the geometry of the scattering experiment and the wavelength of light, so many properties of the input field are seemingly lost because of the complexity of the scattering. However, experiments have shown that when the TM of a scattering material is known, it can be used to measure spectral and polarization properties of input fields[4–6]

The system determination problem is more difficult for a random material because the problem may be ill-posed and the exact configuration of the medium, contained in its TM, is often not interesting. As we will discuss in Chapter 2, even the statistical properties of the output often do not depend on the material properties. However, not all random materials will produce output fields whose statistics are unrelated to the material itself. In Chapter 3, we will experimentally demonstrate the use of the polarization statistics of scattered laser light to distinguish different scattering systems from one another. We will also discuss measurement techniques that do not attempt to extract information about the material directly from the



scattered field but rather from the fluctuations of the scattered field. For example, dynamic light scattering may be used to determine the diffusion coefficient of a suspension of particles; digital speckle interferometry measures local changes in the scattered field to infer strain induced displacements in a sample. We will present a new dynamic light scattering technique that allows for a polarimetric characterization of light by measuring intensity fluctuations after mixing the scattered light with a reference beam that has controllable polarization.

In most common treatments of scattering, a material system is illuminated by a non-random input, i.e. monochromatic laser light. It is also possible to use a randomly fluctuating input field to illuminate a sample and then integrate the transmitted or reflected light for each realization of the illumination. An image of the sample is then formed by correlating the integrated signal with the random illumination patterns. Such correlation imaging (CI) techniques may offer advantages over traditional imaging at low light levels because the detection system integrates all of the collected light onto a single detector rather than spreading it over a detector array. We will carefully examine and compare the performance of CI with traditional imaging modalities under different types of random illuminations.

Finally, in Chapter 5, we will discuss and present several examples of using random materials as measurement devices to estimate the spectral and polarimetric properties of an unknown input. The light scattered from a random material can be thought of as a complicated sampling of the input field. If the sampling function, that is the TM of the material, is known, then the properties of the input field can be recovered from the scattered light. The TM is

learned through a calibration process rather than being set by the choice of optical components, as a result, much of the work of estimating the input field is shifted from the optical components to computational post-processing. One interesting result of this is that the analysis of the scattered light can be adjusted after the light is collected in order to optimize the measurement. Also, because the volume of interaction necessary for the scattering process to randomize the input field may be very small, measurement devices based on the analysis of scattered light can be very compact.

While the random fluctuations of optical fields are often regarded as simply noise to be suppressed, often they contain a wealth of information. This dissertation seeks to highlight situations where randomness may be beneficially exploited, such as imaging in low light levels or making extremely compact and robust optical elements.

## CHAPTER 2: STATISTICS OF RANDOM FIELDS

The scattered field from the most commonly considered class of scattering materials has a uniform phase distribution and a random strength [7,8]. Often the input field is both spatially and temporally coherent, but the resulting output is only temporally coherent because the transfer function is spatially incoherent. For spatially and temporally coherent inputs, the scattered field is often referred to as a speckle pattern [8]. Also, the statistical properties of the output are usually stationary with respect to the location of the input.

The output field at an observation point  $\mathbf{r}$  can be described as the superposition of many fields created by scattering within the medium as

$$\vec{E}(\mathbf{r}, \omega, t) = \sum_i \vec{a}_i(\mathbf{r}, \omega, t) \exp(\vec{\phi}_i(\mathbf{r}, \omega, t)) = \vec{A}(\mathbf{r}, \omega, t) \exp(\vec{\theta}(\mathbf{r}, \omega, t)), \quad (2.1)$$

where  $\vec{a}_i(\mathbf{r}, \omega, t)$  is the field amplitude at the frequency  $\omega$  contributed by the  $i^{th}$  scattering center to the total field at the observation point  $\mathbf{r}$ , and  $\vec{\phi}_i(\mathbf{r}, \omega, t)$  is the phase of the contributed field. The time dependence accounts for the coherence properties of the incident light and any dynamics of the medium. The field amplitude is not expressed directly in terms of the incident field because the scattering centers can also rescatter light from another scattering center, so the exact dependence of  $\vec{a}_i$  on the input field may be very complicated.

To proceed further, we need to make some assumptions about the distribution of the  $\vec{a}_i$ 's and  $\vec{\phi}_i$ 's. The most common set of assumptions to make are that (i) the scattering strength and phase of the each scattering center are independent of the properties of the other scattering centers, (ii) the scattering strength and phase for a given scattering center are

independent of one another, and (iii) the phases are uniformly distributed over the interval  $(0, 2\pi)$  [7,8]. We should point out that the scattering centers are not necessarily individual components of the scattering medium; several individual components can function together as a single effective scatterer or the scattering could result from continuous refractive index fluctuations. Also, because we are assuming a uniform phase distribution, we need to consider a medium in which the light is scattered multiple times before reaching the observation point or is scattered from a large number of scattering centers. Unless otherwise stated, we will be further assuming that the scattering medium is static in time so that any temporal dependence in  $\bar{a}_i$  and  $\bar{\phi}_i$  is due to the incident light and not motion of the scattering centers.

Under the assumptions given, we can calculate the expectation value and standard deviation of the field as well as its probability distribution function. For the sake of convenience, we will only write the equations for one eigen polarization state of the field generated from a temporally coherent source. We begin by separating the field at the observation point into real and imaginary components.

$$E_R(\mathbf{r}, \omega, t) = A(\mathbf{r}, \omega, t) \cos(\theta(\mathbf{r}, \omega, t)) \quad (2.2)$$

$$E_I(\mathbf{r}, \omega, t) = A(\mathbf{r}, \omega, t) \sin(\theta(\mathbf{r}, \omega, t)) \quad (2.3)$$

Because the scattering amplitudes and phases are assumed to be independent, the expectation value of the products in Equations 2.2 and 2.3 will simply be the product of the expectation value of the field and the expectation value of the trig function. Further, the argument of the trig functions is a uniform random variable over the interval  $(0, 2\pi)$ , therefore the expectation value is zero.

$$\langle E_R(\mathbf{r}, \omega, t) \rangle = \langle A(\mathbf{r}, \omega, t) \rangle \langle \cos(\theta(\mathbf{r}, \omega, t)) \rangle = 0 \quad (2.4)$$

$$\langle E_I(\mathbf{r}, \omega, t) \rangle = \langle A(\mathbf{r}, \omega, t) \rangle \langle \sin(\theta(\mathbf{r}, \omega, t)) \rangle = 0 \quad (2.5)$$

Since the real and imaginary parts of the field are zero mean random variables, their variances are simply given by their second moments.

$$\begin{aligned} \sigma_R^2 &= \langle E_R^2(\mathbf{r}, \omega, t) \rangle \\ &= \left\langle \sum_i a_i(\mathbf{r}, \omega, t) \cos(\phi_i(\mathbf{r}, \omega, t)) \sum_j a_j(\mathbf{r}, \omega, t) \cos(\phi_j(\mathbf{r}, \omega, t)) \right\rangle \\ &= \left\langle \sum_i a_i^2(\mathbf{r}, \omega, t) \cos^2(\phi_i(\mathbf{r}, \omega, t)) + \sum_{i,j} \sum_{i \neq j} a_i(\mathbf{r}, \omega, t) a_j(\mathbf{r}, \omega, t) \cos(\phi_i(\mathbf{r}, \omega, t)) \cos(\phi_j(\mathbf{r}, \omega, t)) \right\rangle \quad (2.6) \\ &= \left\langle \sum_i a_i^2(\mathbf{r}, \omega, t) / 2 \right\rangle \end{aligned}$$

The expectation value of the  $\cos(\phi_i(\mathbf{r}, \omega, t)) \cos(\phi_j(\mathbf{r}, \omega, t))$  term factorizes because the cosines are functions of independent random variables. The variance of the imaginary component is the same as the real component. It can also be shown that  $E_R$  and  $E_I$  are uncorrelated in a manner similar to that used in Equation 2.6.

In the regime of heavy multiple scattering the real and imaginary components of the electric field are due to a large number of independent contributions, so their distribution tends to a Gaussian by the Central Limit Theorem. The joint probability density function for a bivariate Gaussian distribution with zero mean, uncorrelated members with the identical variances is

$$p(E_R, E_I) = \frac{1}{2\pi\sigma^2} \exp(-(E_R^2 + E_I^2)/2\sigma^2), \quad (2.7)$$

where  $\sigma^2$  is given by Equation 2.6 [9].

The field cannot be measured directly by optical detectors; the time averaged intensity is usually the only experimentally accessible quantity. Therefore, it will be more convenient to transform Equation 2.7 into a form that contains the magnitude of the electric field and its phase. Using the notation from Equation 2.2, we get

$$p(A, \theta) = \frac{A}{2\pi\sigma^2} \exp(-A^2/2\sigma^2). \quad (2.8)$$

We can see by inspection that the lines of constant probability given by Equation 2.8 are circles centered at the origin; for that reason, variables whose joint probability obey Equation 2.8 are said to obey circular Gaussian statistics—even though Equation 2.8 is a Rayleigh distribution, not a Gaussian distribution. The marginal probability distributions can be obtained by integrating Equation 2.8 with respect to the appropriate variable.

$$p(A) = \int_0^{2\pi} \frac{A}{2\pi\sigma^2} \exp(-A^2/2\sigma^2) d\theta = \frac{A}{\sigma^2} \exp(-A^2/2\sigma^2) \quad (2.9)$$

$$p(\theta) = \int_0^\infty \frac{A}{2\pi\sigma^2} \exp(-A^2/2\sigma^2) dA = \frac{1}{2\pi} \quad (2.10)$$

So, we can see that not only are the real and imaginary components uncorrelated, but because  $p(A, \theta) = p(A)p(\theta)$  they are also independent.

As noted before, we can only measure the time averaged intensity for optical fields. Fortunately, the intensity is a simple function of the field amplitude, and its statistical properties can be derived from the probability distributions of the field. The intensity resulting from Equation 2.1 is

$$I(\mathbf{r}, \omega, t) = \left\langle E(\mathbf{r}, \omega, t) \cdot E^*(\mathbf{r}, \omega, t) \right\rangle_T = \left\langle A(\mathbf{r}, \omega, t)^2 \right\rangle_T. \quad (2.11)$$

Making the substitution that  $A = \sqrt{I}$  in Equation 2.9 and again using the appropriate change of variables, we immediately arrive at

$$p_I(I) = \frac{1}{2\sqrt{I}} p_A(\sqrt{I}) = \frac{1}{2\sigma^2} \exp(-I/2\sigma^2) = \frac{1}{\bar{I}} \exp(-I/\bar{I}), \quad (2.12)$$

where  $p_A$  is the marginal probability distribution for the field given in Equation 2.9, and  $\bar{I}$  is the average intensity of the speckle pattern. Speckle patterns whose intensities follow the distribution in Equation 2.12 are generally referred to as "fully developed" speckle patterns [8]. One property of fully developed speckle patterns is that their contrast, the ratio of their standard deviation to their mean, is 1.

Having established the intensity distribution of the scattered field under certain assumptions, it is also interesting to know the "size" of the speckles in the speckle pattern. The speckle size is usually defined from the first zero of the autocorrelation function of the speckle pattern. For the fully developed speckle patterns that have been discussed so far, the speckle size is

$$\Delta x = \frac{\lambda z}{d}, \quad (2.13)$$

where  $\lambda$  is the wavelength of the incident light,  $z$  is the separation between the scattering medium and the observation plane, and  $d$  is the width of the illuminating beam. Equation 2.12 and Equation 2.13 show very remarkable results; the speckle pattern is a direct result of the interaction of the incident light with the scattering medium, but the fringe spacing and

fringe intensity distribution, if you will, of the interference pattern of the scattered light are not influenced by the properties of the scatterers at all. Of course, it is only the statistical properties of the speckle pattern that are independent of the medium; the actual realization of speckle pattern itself is very sensitive to the precise placement and properties of each scatterer that give rise to the pattern [10–12].

While the preceding discussion was carried out in the spatial domain, the spatial coordinate could simply be replaced with the temporal coordinate to frame the development in terms of dynamic random media and temporal speckles.

Thus far, we have only considered scalar inputs and outputs, but the generalization to vectorial inputs and outputs is straight forward with our assumptions. For scalar outputs, orthogonally polarized inputs will each give rise to a fully developed speckle pattern. If the input is temporally and spatially coherent, which implies fully polarized, the speckle pattern resulting from each input polarization eigen state will add in field to produce a resulting speckle pattern with the statistical properties discussed previously in this section.

If we allow vectorial outputs, the orthogonally polarized output eigen states will be independent of one another both in field strength and phase. Since they are derived from a coherent source, however, the phase difference between them at each point will be constant. The resulting speckle patterns will add in field to produce a speckle pattern that is fully polarized at each point, but they do not interfere because they are orthogonally polarized. As a result, the intensity of the vectorial speckle pattern will be the result of two uncorrelated speckle patterns added on an intensity basis. Because of the intensity addition, the statistics of



the vectorial pattern will deviate from those developed in this section in a known manner; specifically, the intensity will be the sum of two independent random exponentials and the contrast will be  $1/\sqrt{2}$  [8].

The assumption that the resulting scattered field had a uniform, random phase distribution made developing the statistical properties of the output field rather easy. Other types of intensity distributions are possible if the assumptions made at the beginning of the derivation are violated. For example, in low order scattering, the phase may not be uniformly distributed across the entire primary interval. Similar calculations can be carried out for non-uniform phase distributions, although some expressions, such as  $p(A)$ , may not have closed form solutions [8]. Also, the extension to vectorial fields becomes considerably more complicated because there may be correlations between orthogonally polarized output fields.

Physically, the non-uniform phase distribution means that the scattering does not completely remove the spatial coherence of the input, which may be a benefit or a detriment depending on the specific application. In either case, the statistical properties of the scattered field will have not reached the point of being independent of the properties of the scattering medium, so any theoretical development will depend on the specific properties, such as scatterer concentration, of the medium being considered.

The theoretical development of the statistics of random fields seems rather discouraging because the statistics depend primarily on the detection geometry rather than the properties of the material that gave rise to the random field. In spite of that, random fields have been successfully utilized for both of the inverse problems in LST. Some methods for the

material determination problem will be discussed first, followed by the input determination problem.

## CHAPTER 3: MEDIA CHARACTERIZATION

Methods that seek to recover information about the medium that gave rise to the scattered random field typically do not attempt to quantify the TM of the material. While the TM is directly related to the composition and configuration of the random material, it is difficult to extract that information from the scattered field. Instead, the material characterization inverse problem looks for information related to differences in the transfer between two media or fluctuations in the transfer of one medium.

We will focus on three categories of changes in the random material. The first will be random systems that produce partially developed random fields. Because the field statistics are not universal in nature, they may serve as a fingerprint for the material. Second, we will discuss two related techniques for determining the microscopic dynamics in the bulk of a material, dynamic light scattering (DLS) and diffusing wave spectroscopy (DWS). As time progresses, the random system changes and thus alters the entire TM; we will refer to these changes as global dynamics of the TM. We will demonstrate an extension to the DLS and DWS measurements that allows for a polarimetric measurement of the scattered light using a reference beam with controllable polarization.

We will discuss techniques that measure macroscopic changes in the surface of a material. The two methods, digital speckle photography (DSP) and digital speckle interferometry (DSI) examine spatially resolved changes in a surface, so we will refer to these changes as local dynamics of the TM. DSP and DSI are also interesting because they use the TM concept in a reflection geometry. Finally, if the TM of the material does not change, the

scattered field can be made dynamic by changing the input field. Random inputs can be used to form an image of the TM from correlations of the scattered intensity with the input intensities. It will be shown that such correlation images can be superior to traditional images in low light situations.

### 3.1 Statistics of Transfer Matrices

In the Chapter 1, we introduced the TM of a random medium,  $\overline{\overline{T}}$ , using the equation

$$\vec{E}_{out}(\mathbf{r}, \omega, t) = \int_{-\infty}^t \int_{-\infty}^{\infty} \overline{\overline{T}}(\mathbf{r}, \mathbf{r}', \omega, t') \vec{E}_{in}(\mathbf{r}', \omega, t') d\mathbf{r}' dt'.$$

We then argued that, sometimes,  $\overline{\overline{T}}$  does not relate to actual material system itself because of the scattering process causes the spatial and temporal fluctuations of the TM to be Gaussian distributed. However, a field that is partially developed has not yet achieved circular Gaussian statistics, and thus universal, field statistics. Therefore some properties of the material should still be discernible from the direct measurement of the field. Unfortunately, the measured field will depend on those parameters in a very complex way, so it remains difficult to directly determine the material properties themselves; however, partially developed fields can allow discrimination between different materials based on differences in the statistics associated with their TM's.

There are many potential field parameters that could be used to distinguish between different materials: scattered intensity contrast, polarization diversity of the scattered field, and different characteristic length scales of the scattered field. We studied the possibility of using the polarization statistics of light scattered from the surface of a composite material to monitor

its structural modifications. Specifically, we demonstrated that one can distinguish asphalts laid with different pressures. Essentially, we have reduced the complicated random system to a TM that is in fact an effective Jones matrix that will alter, or not, the incident state of polarization. The asphalt system is way too complicated and not much useful information can be determined from a single realization of the TM, However, by examining the statistics of the TM's for many realizations of the complex random media, we have been able to identify systematic differences between them.

While the material systems are similar, there are several factors that could cause them to interact differently with an incident field. For instance, asphalt contains volatile chemicals that will out gas as the asphalt ages, and thus alter the composition of the asphalt and possibly how it interacts with light. Also, the material in the asphalt will deform under the pressure, so different methods of laying the asphalt are likely to result in different porosities and scattering path length distributions.

To simulate two different laying conditions, asphalt was placed in a holder and pressed with either 400 psi or 40 psi. The samples were then illuminated with vertically polarized laser light while the polarization state of a single, scattered speckle was measured; a picture of the set-up is shown in Figure 3.1. To change the speckle seen by the polarimeter, the sample was rotated. Many speckles were recorded in order to measure the spread of the scattered polarization states accurately, and typical results are shown in Figure 3.2. To better simulate real world situations, we performed measurements on wet asphalt and asphalt obscured by sand in addition to uncovered asphalt.



Figure 3.1: Illumination and detection set-up for measuring scattering from asphalt samples.

The Poincare sphere provides a convenient way to visualize the state of polarization of a light field. The Stokes vector,  $[I, Q, U, V]$ , is defined in terms of measured intensities as

$$\begin{aligned}
 I &= I_x + I_y \\
 Q &= I_x - I_y \\
 U &= I_{45} - I_{135} \\
 V &= I_L - I_R.
 \end{aligned} \tag{3.1}$$

The subscripts on the intensities describe the orientation of a polarizer through which the intensity is measured. The L and R subscripts indicate left and right circular polarizers, respectively. Since  $I$  is simply the sum of two intensity measurements through orthogonal polarizers, it gives the total intensity of the light but no polarization information. The remaining

terms,  $Q$ ,  $U$ , and  $V$ , fully describe the polarization state of the light when normalized with  $I$ .

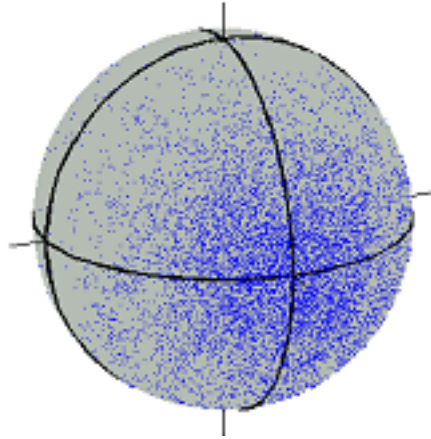


Figure 3.2: Spread of polarization states after scattering from asphalt. -Q polarized light was incident on the sample.

The distribution of points shown on the Poincaré sphere can be characterized by statistics of various orders [13]. In particular, we calculated the first order statistics, the average values of the components of the Stokes vectors, and the second order moments, the average of the squares of the values of the Stokes vectors. The Stokes vector element correlations are essentially intensity-intensity correlations similar to the correlations used in intensity interferometry or dynamic light scattering, for example. Of course many other statistical parameters, such as moments of the cross terms, could be used. Because all of the results are centered about the incident state, -Q, we can use the ratio  $\langle UU \rangle / \langle VV \rangle$  to characterize how symmetric the spread of measured cloud is about the mean. The brackets denote averaging. The results of our measurements are shown in Table 3.1, below.

Table 3.1: Polarimetric properties of different asphalt samples.

	40 psi, clean	400 psi, clean	40 psi, wet	400 psi, wet	40 psi, sand	400 psi ,sand
$\langle Q \rangle$	-0.814	-0.774	-0.816	-0.819	-0.659	-0.674
$\langle QQ \rangle$	0.701	0.656	0.709	0.711	0.553	0.555
$\langle UU \rangle / \langle VV \rangle$	0.862	1.025	1.037	1.025	1.105	1.102

For the clean, dry samples, the measurements indicate that the states of polarization scattered by the highly compressed sample deviate further from the incident state of polarization because they have a smaller  $\langle Q \rangle$ , so the scattered light is more depolarized in a global sense. Also interesting to note is that the polarization states of the less compressed sample spread more anisotropically than the more compressed sample.

In this case, the measurement seems to sample the surface of the sample but not the volume; the TM of the various samples was dominated by surface effects. When the samples are obscured by water or sand, the different compression levels become difficult to distinguish based on our measurements; however, the three surface types, asphalt, water, and sand, are distinguishable from one another based on the average properties of the scattered light, which is to say based on the average properties of their TM's. A different wavelength of light might have interacted more with the bulk of the material and thus would have allowed the TM's of the obscured materials to still show an impact on the scattered polarization states. However, this experiment still clearly demonstrated that when the properties of the TM's are not universal in nature, they can serve as a fingerprint for the material.



### 3.2 Global Transfer Matrix Dynamics

While the statistical properties of random fields can yield some information about the materials that gave rise to them if the field has non-universal statistics, certain properties of the material can be learned even if the scattered field is fully developed. Specifically, to obtain information about the dynamics of the medium, but not about any specific realization of the medium, the dynamics of the random field are of interest.

#### *3.2.1 Dynamic Light Scattering And Diffusive Wave Spectroscopy*

Fields that fluctuate in time are easy to generate with dynamic media, and two related techniques, DLS and DWS, have been developed to analyze such fields [14–22]. The experimental set-ups for both DLS and DWS are the same; polarized laser light is incident on a scattering sample. The light scattered by the sample at an angle  $\theta$  passes through another polarizer and is then collected by a detector. The difference between the two techniques is the nature of the sample as shown in Figure 3.3.

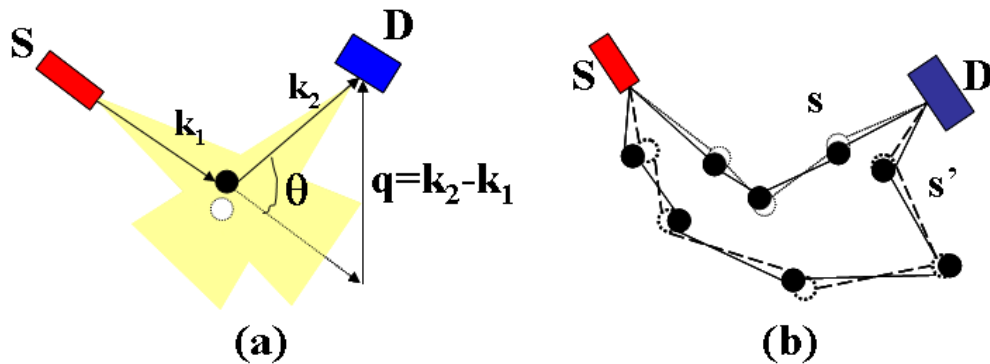


Figure 3.3: (a) The scattered field in DLS is composed of single scattering contributions from many particles. (b) The scattered field in DWS is due to diffusive, multiple scattering.

DLS, also known as quasi-elastic light scattering, assumes that the scattered field is the sum of single scattering contributions from many independent particles, and that the phases of the contributions are uniformly distributed over the interval  $0$  to  $2\pi$ . These two restraints, that the scattered contributions have a uniform phase distribution so that the field is fully developed and that only single scattering be present in the field, make controlling the concentration of the scatterers quite important. DWS, on the other hand, assumes that the detected light has been multiply scattered and can be considered to be diffuse light.

In either case, the autocorrelation of the detected intensity is calculated, and the correlation decay time  $\tau_0$  is related to the motion of the scatterers in the sample. The motion of the scatterers is generally related to the experimentally inaccessible field autocorrelation, but because the scattered field is fully developed, the Siegert relation, Equation 3.2, is used to relate the calculated intensity autocorrelation to the field autocorrelation as

$$\frac{\langle I(0)I(\tau) \rangle}{\langle I(0) \rangle^2} = 1 + \beta \frac{\left| \langle E(0)E^*(\tau) \rangle \right|^2}{\langle I(0) \rangle^2}, \quad (3.2)$$

where  $E(\tau)$  and  $I(\tau)$  are the field and its corresponding intensity at some delay  $\tau$  relative to an initial measurement and  $\beta$  is an experimental parameter, less than 1, given by the ratio of the speckle area to the detector area [14]. The Siegert relation relies on the assumption that the scattered fields are zero mean Gaussian variables, which is an acceptable assumption when the total field is due to scattering from many independent sources.

The primary difference between DLS and DWS is in how the motion of the sample is related to the autocorrelation. In DLS, the autocorrelation can be interpreted in two, equivalent

ways via the Wiener-Khinchine theorem [15]. The first is that the measured intensity does not decorrelate until the scattering particles have traveled distances comparable to the wavelength. Under the assumption that the scatterers are undergoing diffusion and knowing the incident wavelength, the diffusion constant,  $D$ , of the sample can be measured from the time needed for the field to decorrelate [16].

Alternatively, because the scatterers are moving, they will cause a Doppler shift in the frequency of the scattered light. The width of the scattered spectrum can be used to measure the speeds at which the particles are moving and thus the diffusion constant of the medium via the field autocorrelation function. This also means that DLS experiments can be performed by measuring the scattered spectrum directly [14–16], however, because of the added experimental complexity, spectral measurements are generally not done [15]. The measured spectrum and the field autocorrelation are related by

$$S(\theta, \omega) = \int_{-\infty}^{\infty} g^{(1)}(\theta, \tau) \exp(i\omega\tau) d\tau, \quad (3.3)$$

where  $g^{(1)}(\theta, \tau)$  is the autocorrelation of the field scattered into the angle  $\theta$ . Once the field and intensity autocorrelations are known, the diffusion constant,  $D$ , of the material can be found from

$$g^{(2)}(\theta, \tau) = 1 + |C_A(\tau)|^2 \exp(-2q^2(\theta)D\tau), \quad (3.4)$$

where  $g^{(2)}(\theta, \tau)$  is the autocorrelation of the intensity scattered into the angle  $\theta$ ,  $q = (4\pi/\lambda_o) \sin(\theta/2)$  is the difference between the incident and scattered wave vectors, and

$C_A(\tau)$  is the autocorrelation of the particle scattering amplitudes and can be determined from  $g^{(1)}$ .

DWS considers the medium to be divided into a number of independent scattering paths of varying lengths [17–19,22]. The light is thought of using a photon picture, where the photons travel the different paths before reaching the detector. The field autocorrelation can be calculated from

$$g^{(1)}(\tau) \propto \int_0^{\infty} P(s) \exp[-(2\pi/\tau_o)(s/l^*)] ds, \quad (3.5)$$

where  $\tau_o = 1/(Dk_o^2)$  with  $k_o = 2\pi/\lambda_o$ ,  $l^*$  is the transport mean free path, and  $P(s)$  is the probability that the light traveled a path of length  $s$  in the medium. For the particular experimental geometry used,  $P(s)$  is calculated assuming diffusive transport of the light. The appropriate  $D$  is then selected to provide the best fit between the measured and theoretical autocorrelation functions [20,21]. The pathlength distribution  $P(s)$  constitutes the building block of the TM and if fluctuates about some mean value due to the dynamics of scattering centers. The fluctuations in  $P(s)$  cause the TM, and thus the scattered intensity, to vary in time. As a result, the temporal variations of the TM relate to the diffusion coefficient of the scatterers even though each particular realization of the TM tells us nothing about the medium. Recent research has been done to extend DWS to systems with long decorrelation times [20,21], multi-layered media [11], and increase measurement speed [23].

### 3.2.2 Fluctuation Polarimetry

DLS can be extended to quantify the aspect ratio of spheroidal particles as well as the size [24–30]. The detection set-up is modified such that the scattering sample is viewed through a polarizing beam splitter and both of the resulting polarization channels are measured simultaneously [24–28]. In [29,30], the polarization channels are measured sequentially, and a third measurement with the polarizer oriented at  $45^\circ$  is added to project the orthogonal polarization channels onto a common axis. In all cases, the first and second moments of the measured signals, including the cross moment if the polarization channels are measured simultaneously, are calculated and used to infer the shape information for the scattering particles via an assumed analytical or numerical description of the particle scattering.

By measuring the correlations between intensity fluctuations in different polarization states, the extensions of DLS essentially measure the degree of polarization (DOP) of the scattered light. The relationship between intensity fluctuations and DOP was originally recognized in 1960 as an extension to intensity interferometry [31,32]. It is anticipated that more specific and accurate information about the scattering polarizability (particle shape and orientation for instance) could be gained from measuring the state of polarization (SOP) as well. We have recently developed a method for determining both the degree and state of polarization of a randomly fluctuating field by interfering it with an uncorrelated reference beam [33].

Consider a fluctuating, partially polarized E-field where the directions corresponding to the major and minor axes of the polarization ellipse are denoted by  $x$  and  $y$ , respectively. Note

that, in general, the polarization ellipse may be oriented at an angle  $\psi$  with respect to the laboratory frame. Denoting the polarized and unpolarized components of the field with  $P$  and  $U$ , respectively, the field at a point  $\mathbf{r}$  may be written as [34]

$$\mathbf{F}(t) = \left[ \left( P_x(t) \exp(i\phi_x(t)) + U_x(t) \exp(i\phi_x(t)) \right) \hat{x} + \left( P_y(t) \exp(i\phi_y(t)) + U_y(t) \exp(i\phi_y(t)) \right) \hat{y} \right] \exp(i\bar{\omega}t), \quad (3.6)$$

where  $\phi_y(t) = \phi_x(t) \pm \pi/2$ , depending on the handedness of the SOP. In Equation 3.6,  $P_x$  and  $U_i$ , with  $i = x, y$ , are independent random variables which in many cases are Rayleigh distributed, and  $\phi_i$  and  $\phi_x$  are uncorrelated, random phases [8].  $P_y$  is perfectly correlated with  $P_x$  since the SOP is not changing in time. The mean frequency of oscillation of the electric field is  $\bar{\omega}$ . Equation 3.6 can be regarded as the coherent superposition of four “speckle” fields with their amplitudes and phases fluctuating in both space and time [8]; however, the phase of a given speckle is approximately constant when its amplitude is non-zero. The time of constant phase is referred to as the lifetime of the speckle. The relative strengths of the  $P$  and  $U$  components of the superposition determine the intensity statistics of the combined speckle pattern.

Usually, the  $P$ 's and  $U$ 's are considered to be slowly varying envelopes relative to  $1/\bar{\omega}$ , such that one can measure the “short-time” average,  $\tilde{I}$ , that removes the oscillation at  $\bar{\omega}$  but not the fluctuations of the envelope, i.e.,  $\tilde{I}(\mathbf{r}, t) \approx |\mathbf{F}(\mathbf{r}, t)|^2$  (see page 100 in [9]). This is often, and somewhat misleadingly, referred to as the “instantaneous” intensity, a convention that we

will, however, follow for the rest of this Letter. We will omit the tilde from all subsequent intensities.

For E-fields whose components are Gaussian random variables, the second moment of the intensity fluctuations at a point  $\mathbf{r}$  is given by [34]

$$\langle (\Delta I(\mathbf{r}, t))^2 \rangle = (1 + D^2) \langle I(\mathbf{r}, t) \rangle^2 / 2, \quad (3.7)$$

where  $D$  is the DOP,  $\langle I(\mathbf{r}, t) \rangle$  is the average intensity of the light at the point  $\mathbf{r}$ ,  $\Delta I(\mathbf{r}, t) = I(\mathbf{r}, t) - \langle I(\mathbf{r}, t) \rangle$ , and  $\langle \rangle$  denotes “long-time” averaging. This relationship means that the contrast of the intensity fluctuations (i.e. the second moment normalized to the mean) is, in fact, given by the amount of correlation between the orthogonal E-field components, i.e., the DOP. This is analogous to determining  $D$  by measuring the fluctuations in two, orthogonally polarized channels at the same time, as is frequently done, and calculating the cross-correlation between the measurements.

Unfortunately, it is not possible to determine the SOP from the fluctuations of the instantaneous intensity. This is because the SOP depends on the phase between the polarized E-field components, which would require time resolution better than  $1/\bar{\omega}$  to measure directly in the intensity fluctuations. We can, however, go further if we bring in a reference field,  $\mathbf{R}$ . We will choose the reference to have a non-fluctuating intensity with the same mean frequency as  $\mathbf{F}$ . For simplicity, this reference will be a linearly polarized field whose orientation,  $\alpha$ , can be controlled at will. Most importantly, because of the random nature of the phases in Equation 3.6, this reference can be incoherent with respect to the fluctuating field, meaning that no

stable interference is observed when  $\mathbf{R}$  and  $\mathbf{F}$ , or any component of  $\mathbf{F}$ , are superposed. Nevertheless, during the lifetime of a single speckle, the two fields are able to interfere. If the fluctuating field is fully polarized along the same direction as the reference, the resulting intensity statistics follow a Rician distribution [8]. In general, the statistics are more complicated because the intensity fluctuations arising from the polarized components of the fluctuating field will be partially correlated based on the SOP of the fluctuating field. However, as we will show below, the full polarimetric description for the field  $\mathbf{F}$  can be recovered by measuring the intensity statistics of the superposition as the polarization orientation of the reference field is changed.

If the intensity of the linearly polarized reference field is  $|\mathbf{R}|^2$ , the instantaneous intensities along the major and minor axes of polarization ellipse of  $\mathbf{F}$  will be denoted as

$$\begin{aligned} |R_x(\alpha)|^2 &= |\mathbf{R}|^2 \cos^2(\psi - \alpha) \\ |R_y(\alpha)|^2 &= |\mathbf{R}|^2 \sin^2(\psi - \alpha) \end{aligned} \quad (3.8)$$



The instantaneous intensity of the fluctuating field can be decomposed into four parts: a polarized and an unpolarized intensity along both x and y-axes. These following relations will hold for the intensities:

$$\begin{aligned}
D\langle |\mathbf{F}|^2 \rangle &= \langle P_x^2 \rangle + \langle P_y^2 \rangle \\
(1-D)\langle |\mathbf{F}|^2 \rangle &= \langle U_x^2 \rangle + \langle U_y^2 \rangle \\
P_y^2 / P_x^2 &= A \\
\langle U_y^2 \rangle / \langle U_x^2 \rangle &= 1
\end{aligned} \tag{3.9}$$

The first two equations simply mean that the (un)polarized component of the intensity is the sum of the (un)polarized intensities along both axes of the polarization ellipse [34]. The third relation defines the square of the ellipticity of the polarization ellipse, which is constant during the measurement. Consequently,  $0 \leq A \leq 1$  since the semi-minor axis of an ellipse is by definition non-negative and smaller than the semi-major axis. The unpolarized intensities, though, must be equally divided between the two axes upon long-term averaging as shown in the last relation in Equation 3.9; however, the ratio of the instantaneous unpolarized intensities is unbounded because they fluctuate in an uncorrelated manner [34].

In the superposition of  $\mathbf{R}$  and  $\mathbf{F}$  fields, the instantaneous intensity can be expressed as

$$\begin{aligned}
I_i(\alpha) = & P_i^2 + R_i^2(\psi - \alpha) + U_i^2 + 2P_iR_i(\psi - \alpha)\cos(\phi_i) \\
& + 2P_iU_i\cos(\phi_i - \varphi_i) + 2U_iR_i(\psi - \alpha)\cos(\varphi_i) ,
\end{aligned} \tag{3.10}$$

where  $i = x, y$ . Since the phases in Equation 3.10 are random, the first moment of  $I(\alpha)$  is simply

$$\langle I(\alpha) \rangle = \langle |\mathbf{F}|^2 \rangle + \langle |\mathbf{R}|^2 \rangle \tag{3.11}$$

and, using Equation 3.9, the second moment is given by

$$\begin{aligned} \langle (\Delta I(\alpha))^2 \rangle = & \langle |\mathbf{F}|^2 \rangle^2 \left[ (1 + D^2) / 2 \right] + \langle |\mathbf{F}|^2 \rangle \langle |\mathbf{R}|^2 \rangle \{ (1 - D) \\ & + 2D \left[ 1 + (A - 1) \sin^2(\psi - \alpha) \right] (1 + A)^{-1} \}. \end{aligned} \quad (3.12)$$

Finally, using the calculated moments one can evaluate the contrast of the intensity fluctuations as

$$C(\alpha) = \sqrt{\langle (\Delta I(\alpha))^2 \rangle} / \langle I(\alpha) \rangle \quad (3.13)$$

Equation 3.12 constitutes the main result of our derivation; it shows that the intensity fluctuations of the superposition depend on  $D$ ,  $A$ , and  $\psi$ , which provide all of the single point polarimetric information, up to the handedness of the polarization ellipse. The exact form of Equation 3.12 relies on the Gaussian nature of the fields (we used  $\langle X^2 \rangle = 2\langle X \rangle^2$  with  $X = P_i^2, U_i^2$ ) however, similar relationships can be derived for fluctuations obeying other distributions.

The first term in Equation 3.12 shows that we recover Equation 3.7 when the reference is not present, as expected. The second term in Equation 3.12 highlights the interferometric nature of the measurement at short time scales; it is the “interferometric gain” that comes from mixing the reference and fluctuating fields [1]. While  $C$  decreases as  $1/|\mathbf{R}|$  for  $|\mathbf{R}| \gg |\mathbf{F}|$ , the actual magnitude of the intensity fluctuations increases as  $|\mathbf{R}|$ . The ability to alter the strength of the intensity fluctuations in a controllable manner may prove very useful for measurements on weak fields.

Determining the unknown Stokes vector from the values of the measured contrasts requires the use of numerical techniques because, while closed-form solutions for the variables in Equation 3.12 exist, the equations are transcendental. Fortunately, the solution domain is finite with  $A \in [0,1]$ ,  $\psi \in [0, \pi)$ , and  $D \in [0,1]$ . In principle,  $D$  can be determined by simply measuring the intensity fluctuations without the reference field and then applying Equation 3.7, thus reducing the problem dimensionality.

The Stokes vector may be defined in terms of  $[A, D, \psi]$

$$\begin{aligned}\chi &= \tan^{-1}(\sqrt{A}) \\ s_1 &= D \cos(2\psi) \cos(2\chi) \\ s_2 &= D \sin(2\psi) \cos(2\chi) \\ s_3 &= D \sin(2\chi)\end{aligned}\tag{3.14}$$

where  $\chi$  is the ellipticity angle [35]. The uniqueness of the calculated Stokes can also be demonstrated by noting that Equation 3.12 has the form  $G(A,D) + H(A,D) \sin^2(\psi - \alpha)$ . If there is any another combination of  $A$  and  $D$  such that  $G(A,D) = G(A',D')$  and  $H(A,D) = H(A',D')$ , then an identical  $C(\alpha)$  would be obtained for multiple polarization states. However, the only non-trivial solution to these two equalities is  $A' = 1/A$  and  $D' = -D$ , both of which are non-physical. As a result, we can concluded that  $C(\alpha)$  is in fact uniquely determined by  $A$  and  $D$ , and that finding the  $A$  and  $D$  that produce the best fit to the measured data will yield the correct SOP.

The concept was tested experimentally on a fluctuating field created using two rotating diffusers illuminated by a laser beam. To minimize the effects of detector averaging, a polarizer

was placed after one of the diffusers while the other was blocked, and then the rotation rate of the unblocked diffuser was adjusted to ensure that the intensity of the scattered light followed a negative exponential distribution. Both diffusers were adjusted in the same manner. A polarizer and quarter waveplate were placed after one of the diffusers to create a fully polarized fluctuating field. The other diffuser created an unpolarized fluctuating field that was added the polarized fluctuating field to control D. The reference field was obtained by diverting a small part of the initial beam before the diffusers, and the total fluctuating intensity, i.e. the intensity of the overlapped polarized, unpolarized, and reference fields was measured using a photodiode. The set-up is shown in Figure 3.4.

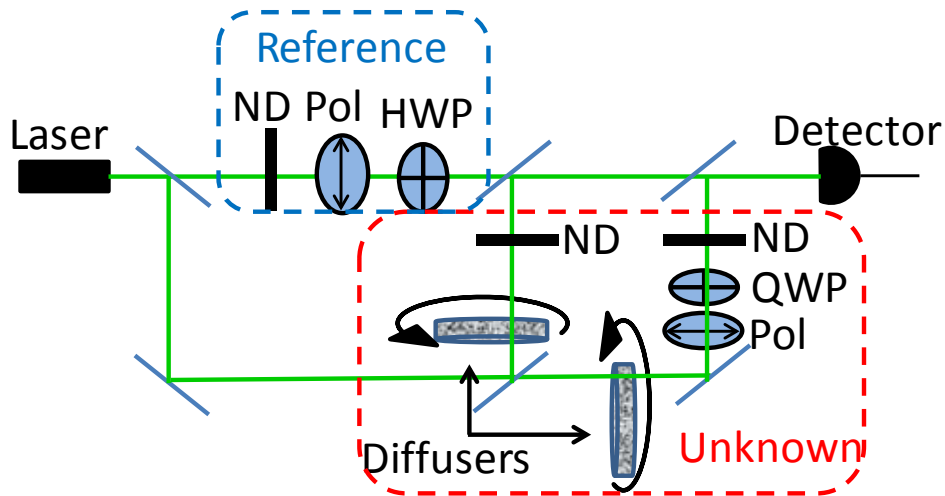


Figure 3.4: The set-up used to test the fluctuation polarimetry theory. The abbreviations are ND for neutral density filter, Pol for polarizer, QWP for quarter waveplate, and HWP for half waveplate.

Figure 3.5 clearly shows a strong dependence of the contrast on the SOP of the fluctuating field, rather than just its DOP. Each of the experimental contrasts was calculated by recording approximately 500 intensity speckles. The variation between contrasts from different realizations of 500 speckles is smaller than the symbols in the figure. The contrasts calculated

from the measured intensity fluctuations (dots) and from Equation 3.13 (lines) are shown for several different fluctuating fields. The lines were obtained by finding the  $D$ ,  $A$ , and initial  $\theta$  that produced the best fit to experimental contrasts. After determining  $D$ ,  $A$ , and  $\theta$ , Equation 3.14 was used to calculate the normalized Stokes vectors for each case, and the results are shown for the corresponding plots in Figure 3.5. The measured Stokes vectors are in good agreement with standard measurements using a polarizer and quarter waveplate.

While Equation 3.7 cannot be applied to our measured intensity fluctuations because the reference field makes the underlying statistics of the total field non-Gaussian, it is still instructive in understanding the results shown here. In our experiment, the DOP's of both the fluctuating and the reference fields are constant, but the DOP of the total field depends on the orientation of the reference field with respect to the polarization ellipse of the fluctuating field. For example, if the fluctuating field is linearly polarized, then the total field remains fully polarized when the reference field is aligned with the fluctuating field. As the orientation of the reference field is changed, however, the DOP of the total field, and thus the resulting intensity fluctuations, decreases because the two fields are incoherent with one another.

We have demonstrated a method for extracting the state of polarization of a fluctuating field from the first two moments of the distribution of intensity fluctuations after mixing the fluctuating field with an uncorrelated reference field. The short-term interferences between these fields influence the intensity fluctuations in a manner that depends on the state of polarization of the fluctuating field. Analyzing the residual state of polarization of optical fields is of interest for a number of sensing applications that rely on light scattering. Our technique

may prove to be particularly interesting for DLS and DWS measurements where the intensity fluctuations of scattered light are already being measured. Most polarimetric techniques require either discarding part of the light of interest due to the use of polarimetric filters or splitting the light among multiple detectors; however, by adding a reference and measuring the intensity fluctuations of the mixed field, the SOP of the signal can be determined without splitting or discarding any of the signal light. In addition, because the method is interferometric in nature it may especially appropriate for measurements of weakly scattering systems.

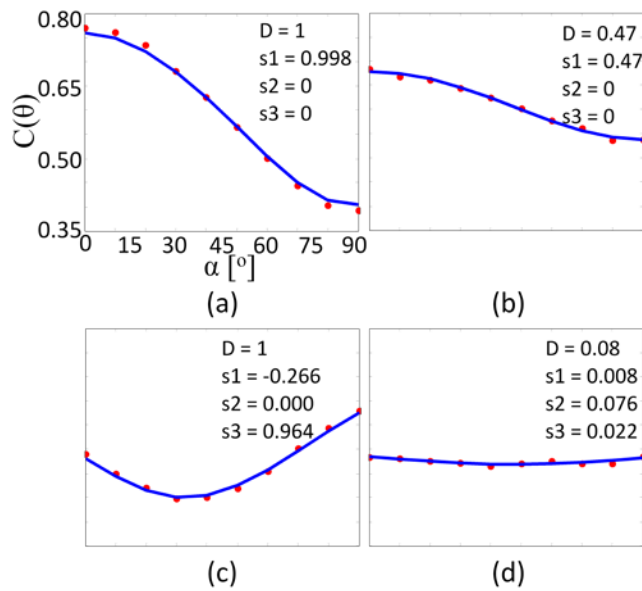


Figure 3.5. The experimental (red dots) and theoretical (blue line) intensity contrasts for (a) vertically polarized, (b) partially vertically polarized with  $D \approx 0.455$ , (c) elliptically polarized, and (d) unpolarized fluctuating fields as a function of the orientation of a linearly polarized reference field. All of the plots are on the same scale. The DOP and Stokes vector for the best fit to the experimental contrasts are indicated for each plot.

### 3.3 Local Transfer Matrix Dynamics

We will now turn from correlations of temporal varying TM's to consider TM's that fluctuate in the spatial domain.

#### *3.3.1 Digital Speckle Photography And Digital Speckle Interferometry*

One of the earliest practical techniques for utilizing the random scattering from materials was digital speckle photography (DSP) [36]. DSP attempts to characterize in-plane deformations of a surface as a strain is applied to it. The set-up needed to characterize the deformations is comparatively simple, see Figure 3.6. A rough surface is coherently illuminated by a quasi-monochromatic point source or an expanded laser beam. The surface is imaged onto a detector array, so that when the surface is illuminated, the speckle pattern at the surface is recorded.

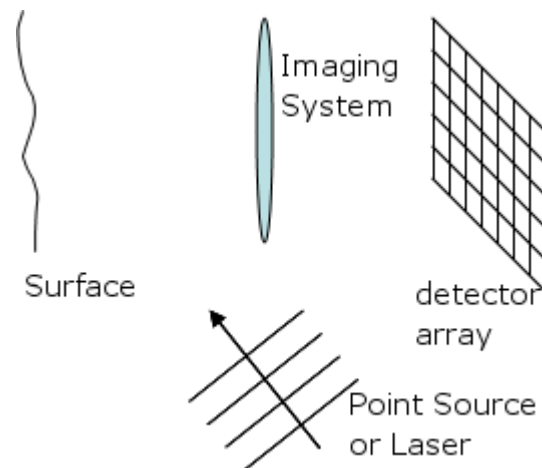


Figure 3.6: Basic set-up to perform speckle photography. A surface is coherently illuminated by a point source or laser. The speckle pattern at the surface is imaged onto a detector array by a lens system.

The analysis is performed by recording the speckle pattern generated by the surface in an unstressed state. Strain is then applied to the surface, and a new speckle pattern is

recorded. Under the assumption that the surface did not change too much when the stress was applied, the cross-correlation can be used to describe the shifts between the two patterns. The cross-correlation for two fully developed speckle patterns is given by

$$\langle I_1(\mathbf{x}_1)I_2(\mathbf{x}_2) \rangle = \langle I_1(\mathbf{x}_1) \rangle \langle I_2(\mathbf{x}_2) \rangle + |\langle E_1(\mathbf{x}_1)E_2^*(\mathbf{x}_2) \rangle|^2, \quad (3.15)$$

with

$$\langle E_1(\mathbf{x}_1)E_2^*(\mathbf{x}_2) \rangle \propto \delta(\mathbf{x}_1 - \mathbf{x}_2), \quad (3.16)$$

where  $I_1$  and  $I_2$  are the speckle patterns for the stressed and unstressed surface, the  $E$ 's are the corresponding field distributions, and  $*$  denotes the complex conjugate [36]. Because the speckles on the surface of the material are being imaged, their movements give the movement of the underlying surface directly.

Cross-correlating the speckle patterns will only give a net shift of the stressed pattern with respect to the unstressed pattern, which is not the quantity of interest. So, the two patterns are divided into sections as shown in Figure 3.7, and each section is then cross-correlated with the corresponding section in the other image. Individual speckles are not tracked because they can be annihilated and new speckles created as the speckle pattern moves [37]. The shifts of all of the sections are then combined into a flow field map to visualize the deformations of the entire surface.

DSP also provides additional information about the surface deformations because the value of the correlation function is determined. If the speckle pattern undergoes a pure translation, then it will be fully correlated with itself; however, shears or local rotations of the speckle pattern will cause some decorrelation between the speckle patterns. The decorrelated



areas correspond to plastic regions of the test sample, which are more prone to mechanical failure [36].

Slightly after the introduction of DSP, digital speckle interferometry (DSI) was introduced. DSI was originally used to measure out of plane displacements, but has been generalized to measure surface displacements in all directions [36]. DSI is similar to DSP in that a test surface is illuminated with a coherent light source and the resulting speckle pattern is recorded; however, in DSI the speckle pattern generated by the test surface is interfered with a reference beam. The reference is generally a plane wave, a speckle pattern generated from a master surface, or a second beam illuminating the test sample (for measuring in plane displacements). A basic set-up for measuring out of plane displacements is shown in Figure 3.8.

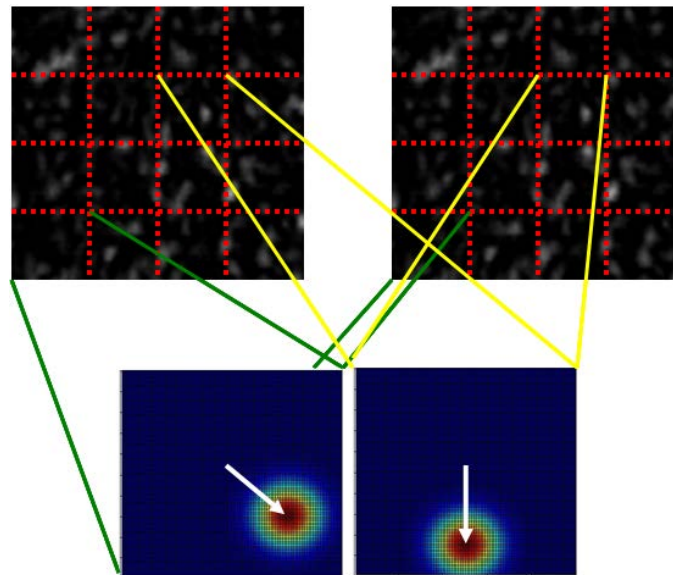


Figure 3.7: Cross-correlating sections of two speckle fields gives the local shift of the speckle patterns. The local shifts can be used to generate a flow map of the surface to visualize the local in-plane shifts.

In most cases, the reference surface is assumed to constant during the measurement. The test surface is loaded and a new speckle pattern is recorded for each load level. The

structure of the speckle pattern is assumed to be unchanged when small loads are applied to the surface, but the phase difference between the test and reference beams will change due to small, strain-induced changes in the surface height. The measured intensity will be

$$I = I_{ref} + I_{test} + 2\sqrt{I_{ref}I_{test}} \cos(\phi + \phi(\Delta h)), \quad (3.17)$$

where  $I_{ref}$  is the intensity of the reference,  $I_{test}$  is the intensity from the test surface,  $\phi$  is the phase difference between the unstressed test surface and the reference, and  $\phi(\Delta h)$  is the added phase due to the change in the surface height. The phase can be determined by adding known shifts to the reference, by using a piezoelectric transducer to shift the reference for example [36].

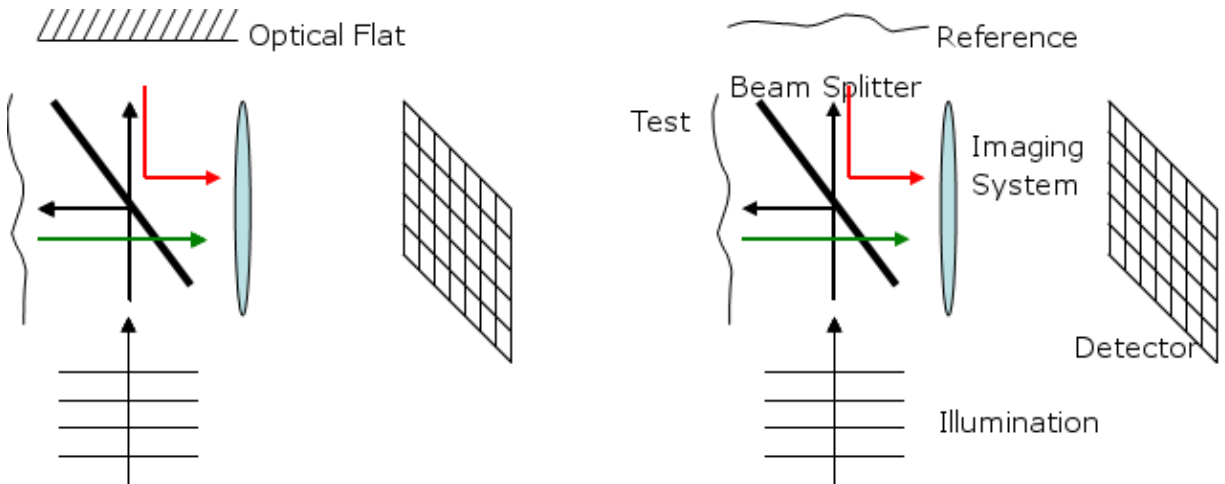


Figure 3.8: Basic set-up to perform speckle interferometry. A surface is coherently illuminated by a point source or laser. The speckle pattern generated by the surface is interfered with a reference beam or a speckle pattern generated by a reference surface. The speckle pattern at the surface is imaged onto a detector array by a lens system.

DSI can also be used to measure in plane displacements of the test surface. Figure 3.9 shows a simple version of the measurement set-up. The test surface is illuminated by two plane

waves at an equal angle,  $\theta$ , from the average surface normal. When the test surface is strained, the phase change due to out of plane displacements will be equal in both beams and thus not cause a change in the measured intensity. Similarly, in-plane displacements that are perpendicular to the plane containing the illumination beams will not produce a phase shift; however, in-plane displacements in the plane containing the illumination beams will produce a change in the interference pattern. The phase shift is given by

$$\Delta\phi = \frac{4\pi}{\lambda} \Delta x \sin(\theta), \quad (3.18)$$

where  $\Delta x$  is the magnitude of the shift, and  $\lambda$  is the wavelength of the illumination.

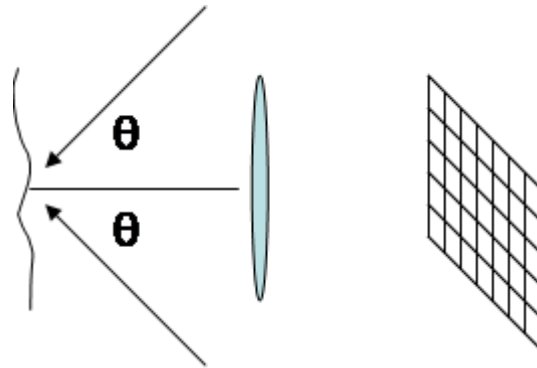


Figure 3.9: Experimental geometry for measuring in plane surface displacements. The test surface is illuminated by two plane waves at an equal angle  $\theta$  from the average surface normal.

Several, more complicated schemes for measuring in plane displacements in all directions have been developed. They consist primarily of using two, orthogonal pairs of beams either sequentially with a single detector or simultaneously with two detectors and the beam pairs orthogonally polarized. Measurement devices have also been constructed combining in plane and out of plane measurements to measure the total displacement of the surface. For a thorough review of DSI and DSP see [36].

### 3.3.2 Correlation Imaging

While DSP and DSI have been extensively developed and have generated commercial products, a number of other applications of randomly scattered light to characterize the scattering material have been discussed and demonstrated on the laboratory scale. Several types of microscopy systems illuminate a sample with a random field and measure the scattered field. Aperture correlation microscopy does this to achieve confocal microscopy axial, ideally with reduced measurement time [38]. A random illumination is used in double pass fashion to act like an effective array of confocal pinholes [38,39]. Mertz uses fluctuating illumination to improve sectioning in a wide field microscope by forming a fluorescence image based on the rms fluctuations of the returned signal [40,41].

The techniques in the last paragraph all form an image directly using spatially resolved detection and so require modestly high photon fluxes for good imaging performance. Another class of imaging systems uses random illumination patterns integrated onto a bucket detector. The image is then formed using either compressive sensing techniques or correlating the integrated signal with the random process formed by each pixel through the series of random illuminations [42–44].

Compressive sensing based techniques offer an advantage over traditional imaging in that images of reasonable quality can be formed from an undersampled version of the desired image, thus reducing requirements on data acquisition and storage [43]. Correlation imaging (CI) research is often justified either to elucidate the relationship between classical and quantum correlations or by the simplicity of the detection scheme [44–47]. We will

demonstrate that CI using classical correlations can offer improved imaging performance over traditional imaging in situations of low brightness illumination and low target reflectivity because of the integration of the scattered light onto the single detector.

The imaging performance of CI systems has been studied extensively assuming thermal illumination, usually with the assumption that the field's correlation properties follow a Gaussian-Schell model [47–50]. The Gaussian-Schell model allows theoretical results to be derived for various system performance measures, such as resolution and SNR. The detected field is quantized to account for detector shot noise, but other noise sources are generally neglected. The field is treated classically for purposes of reflecting off of the target and being absorbed by the detector, that is to say that both processes are treated as a multiplicative factor that reduces the average intensity but does not introduce any additional intensity fluctuations. However, in the limit of low fluxes, the partitioning of the photon stream during reflection and absorption, due to sub-unity reflectivity and quantum efficiency, respectively, can significantly reduce the correlation between the detected intensity and the random illumination patterns.

We used numerical experiments to evaluate the performance of CI against traditional imaging in low flux situations. The process of generating the numerical data uses three different types of illumination and is outlined in Figure 3.10. An ensemble average is generated by using 10,000 realizations for each type of illumination. First, the illumination is realized using a fully developed speckle pattern of intensities generated in the far-field of a two dimensional array of point sources having random initial phases.

Another random intensity pattern was generated using random distribution of points that were convolved with a Gaussian blur function. The width of the Gaussian blur was chosen such that the spatial autocorrelation of the intensity pattern is very similar to that of the speckle patterns. In CI, the spatial autocorrelation of the illumination intensity governs the resolution of the image. Equation 3.19 shows the value of the correlation function at the point  $\mathbf{x}$ ,

$$C(\mathbf{x}) \propto \int \left\langle I_p(\mathbf{x}, t) I_p(\mathbf{x}', t) \right\rangle_t R(\mathbf{x}') d\mathbf{x}' \quad (3.19)$$

$I_p$  is the intensity pattern illuminating the sample and  $R$  is the sample reflectivity or transmittance, and the brackets are averages over time [51]. The bracketed quantity in Equation 3.19 represents the average size of a spot in the random illumination, and the highest resolution image is achieved when this quantity decreases quickly as a function of  $\mathbf{x}'$  [8].

Of course, because the number of points in each illumination pattern is controllable, the spatial density of nonzero intensities can also be controlled. In this numerical experiment, the second and third types of illumination use densities of 1% and 20%, respectively.

The numerical experiment was conducted following the major steps described in Figure 3.10. To facilitate the comparison between different imaging scenarios, each random illumination pattern is normalized such that the integrated area of each illumination spot is unity; this is of course only approximately true for the fully developed speckles since they are irregularly shaped and often connected. The normalization was chosen such that the values could be interpreted as the distribution of energy in that spot. The normalized illumination pattern is then multiplied by a factor to represent the average number of photons in a speckle.

Finally, the average number of photons was used as the rate parameter for a Poisson distribution. The Poisson sampled image represents the incident photon stream for a given illumination pattern.

We examined two different illumination levels. The first was such that, on average, there is one photon per speckle per pattern. Illuminating with one photon per speckle, under the three different types of illumination described before, results in different photon fluxes incident on the target. Since the results of imaging with a CCD are expected to depend on the integrated photon flux per pixel, the correlation images would be then compared to CCD images of different quality. To facilitate the comparison to standard imaging, we also set the photon fluxes to be the same for each illumination type.

Next, the photon stream is partitioned using the reflectivity of the sample. For each photon, a Bernoulli trial is performed with probability of success given by the sample reflectivity at that point. The result is, of course, that the reflected photon stream at each point is the incident photon stream sampled by a binomial random variable.

Finally, the reflected photon stream is detected. The detection process is handled as another binomial random sampling with a probability of each reflected photon being absorbed given by the detector's quantum efficiency.

We considered four different detection scenarios under realistic conditions. The first is spatially resolved detection by a cooled CCD camera. The quantum efficiency of the camera was 0.9. In the low light level regime, the camera's read noise is a significant source of noise, so each pixel is given an additive Gaussian random variable with a mean and variance of 15 counts.

Because the CCD resolution is matched to the target, which is higher than that of the correlation images, the second case considered is the CCD image blurred with the same Gaussian spot used for some of the illumination patterns. The blurring matches the resolution of the CCD to the correlation images while suppressing the noise in the image.

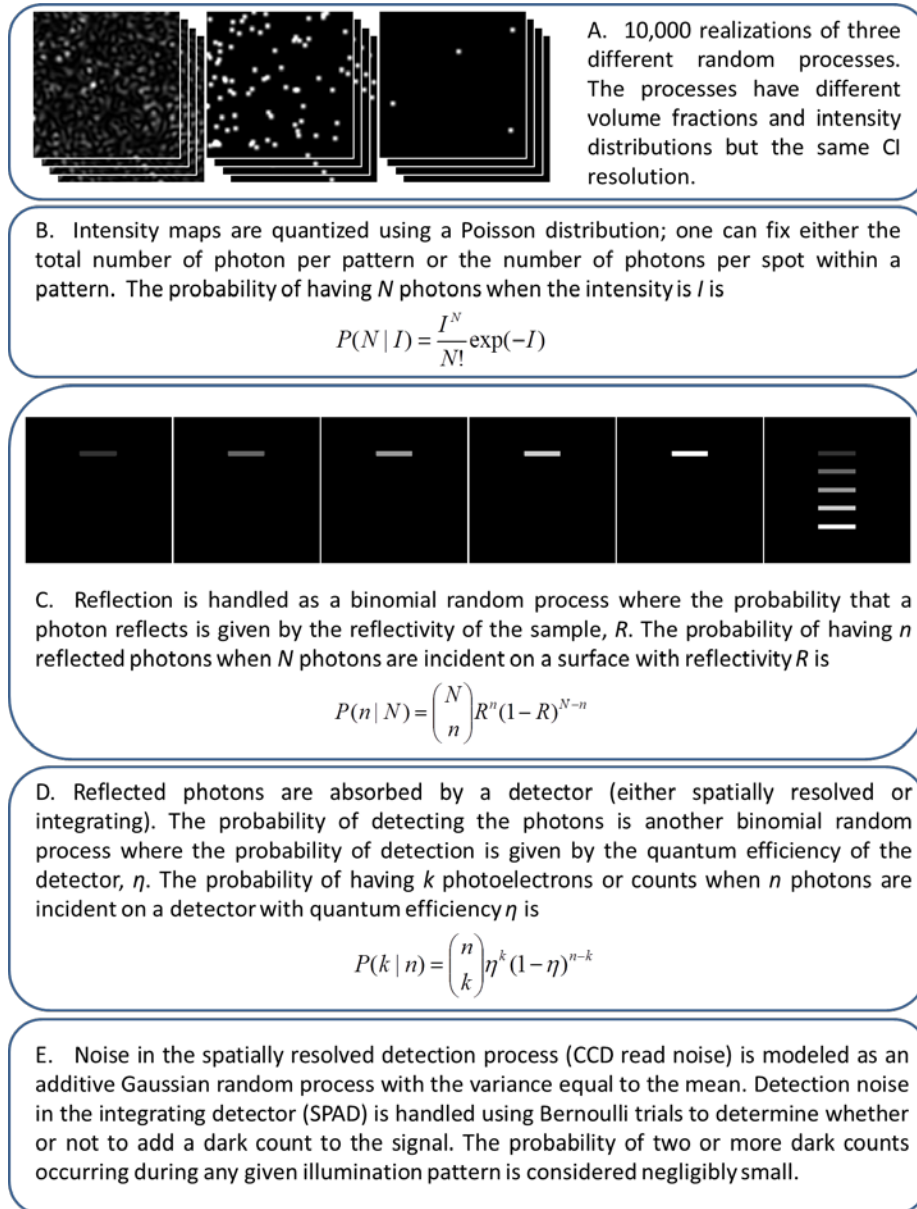


Figure 3.10: Steps taken in the numerical experiment to compare CI with traditional, spatially-resolved CCD based imaging.



The third detector scenario uses a single photon avalanche photodiode (SPAD) with a quantum efficiency of 0.5. In this case, for the simulated photon fluxes, the dominant source of noise is dark counts, so 15 dark counts were added at random to the integrated signal. The fourth case is that of an ideal photon counter with no dark counts and unity quantum efficiency so that the impact of a non-ideal detector may be seen more clearly.

All of the quantum efficiency and noise parameters are typical for the performance of currently available detectors. For the purposes of noise calculations, we assume that data collection takes 1 second, which is within the capabilities of current micromirror arrays.

We used six different targets to evaluate the performance of the different illumination and detection conditions. One target consisted of five stripes with reflectivities of 0.2, 0.4, 0.6, 0.8, and 1, respectively, as illustrated in Figure 3.11(d). Because CI should be influenced by the total area of the target, we have also considered targets consisting of individual stripes imaged one at a time. Each stripe had a width of 5 pixels, a length of 40 pixels, and a separation of 20 pixels. The Gaussian illumination spots had a standard deviation of 2 pixels and were truncated at a diameter of 8 pixels. Typical realizations of different types of illumination patterns are shown in Figure 3.11(a)-(c).

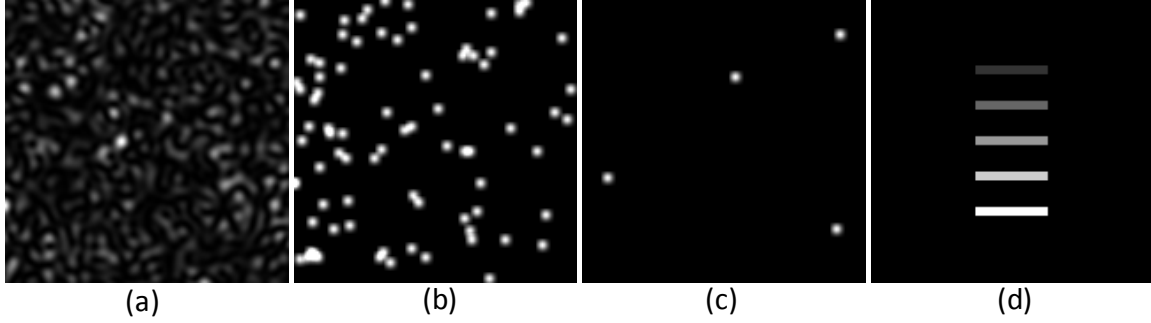


Figure 3.11: Single realizations of the random illumination patterns for (a) fully developed speckle pattern, (b) and (c) Gaussian spots covering 20% and 1% of the illuminated area, respectively. (d) Target consisting of five stripes with reflectivities of 0.2, 0.4, 0.6, 0.8, and 1. The single stripe targets used stripes of the same dimensions located at the position of the top stripe in (d).

Two metrics are used to quantify the quality of the images. The first is the contrast of the targets defined as

$$C(\mathbf{A}) = \frac{\sqrt{\langle (S(\mathbf{x}) - \langle S(\mathbf{x}) \rangle_{\mathbf{A}})^2 \rangle_{\mathbf{A}}}}{\langle S(\mathbf{x}) \rangle_{\mathbf{A}}}, \quad (3.20)$$

where  $S(\mathbf{x})$  is the signal at the location  $\mathbf{x}$ , i.e., either the detected intensity or the value of the correlation, and the brackets represent an average taken over the area,  $\mathbf{A}$ , of a stripe. The contrast is a measure of how much the image is fluctuating over the target area but does not indicate how easily the targets can be differentiated from the background. The second descriptor is the visibility of the targets defined as

$$V(\mathbf{A}) = \frac{\langle S(\mathbf{x}) \rangle_{\mathbf{A}} - \langle S(\mathbf{x}) \rangle_{\mathbf{B}}}{\sqrt{\langle (S(\mathbf{x}) - \langle S(\mathbf{x}) \rangle_{\mathbf{B}})^2 \rangle_{\mathbf{B}}}}. \quad (3.21)$$

The  $\mathbf{B}$  subscript indicates averaging over the background area. The visibility measures the separation between the target and the background signals normalized to the fluctuations in the

background.

The results for the illumination patterns having the same photon flux are summarized in Table 3.2. The columns for the CCD performance are averaged over the three illumination patterns because, as expected, there was little variation of the performance of the CCD based on the type of random illumination. One of the most striking results relates to the visibilities of the 1% coverage illumination targets. The visibility of CI at low light levels improves as the number of active illumination spots in the pattern decreases even though the total number of photons is the same. We attribute this behavior both to the reduced number of random processes contributing to the integrated intensity and to the fact that for a constant total number of photons per pattern, the number of photons per spot increases as the number of active spots decreases.

The fluctuations of the incident photon stream are the result of two processes. The first is the random nature of the photon arrival times, which follows a Poisson distribution for constant intensity sources. These fluctuations are referred to as shot noise or photon noise. The second source of fluctuations is due to the varying intensity of the incident illumination that will be used to form the correlation image; these fluctuations are referred to as wave noise, although they are actually part of the signal. Typically, the strength of the shot noise and the wave noise have a different dependence on the average photon flux that causes wave noise to dominate at high flux levels and shot noise to dominate at low flux levels. The relative importance of the two noise sources as a function of photon flux is the key to understanding why the 1% coverage illumination patterns produce the greatest visibilities of the three

correlation images. As the number of photons per illumination spot increases, the fluctuations in the spot intensity become dominated by the wave noise, which is actually the signal.

The visibility of the correlation image CI will not improve significantly with the number of photons once the intensity fluctuations are dominated by wave noise. The visibility of the CCD image, on the other hand, should increase linearly with the number of detected photons because the background areas in the CCD image only suffer from read noise, which is independent of the signal level. Typically, the only way to improve the visibility of CI is to reduce the fluctuations of the correlation in the background by increasing the number of illumination patterns. However, we have shown that the visibility of CI depends strongly on the nature of the random illumination, and that the visibility can be improved significantly by reducing the amount of the target illuminated at any given time.

From the data in Table 3.2, it is not apparent how much of the improvement in the CI visibility is due to changing the coverage area of the illumination and how much is due to the change in the unwanted noise in the illumination that changing the coverage area causes. If, instead of fixing the number of photons per pattern, we maintain constant the number of photons per speckle in order to keep the noise characteristics the same, we find that the CI visibility is only weakly dependent on the coverage of the illumination. Also, we note that, due to the increased number of photons used to form the image, the standard imaging quickly dominates the correlation imaging CI as the speckle volume fraction increases. At low volume fractions, however, the visibility of the correlation image is superior, as in the previous case, as shown in Table 3.3.

Table 3.2: Visibility and contrast when a single stripe target is imaged using CI and a conventional CCD with a constant number of photons per illumination pattern. R is the stripe's reflectivity, and N is the number of photons reflected from the stripe. CCD is calculated from the spatially resolved detection of the reflected photons, and Blurred is from the same image but with the Gaussian blur kernel applied as described in the text. The results in the "CCD" and "Blurred" columns represent the average for the three types of illumination. The remaining columns contain the results corresponding to the bucket detectors. "Ideal" indicates an ideal photon counter while "SPAD" denotes the single photon avalanche photodiode. In the CI case, the performance depends on the illumination. "Speckle", "20%", and "1%" correspond to the three types of illumination discussed in text: fully developed speckle patterns and the Gaussian spots with 20% and 1% coverage, respectively.

Visibility (higher is better)									
R	N	CCD	Blurred	Ideal, 20%	SPAD, 20%	Ideal, 1%	SPAD, 1%	Ideal, speckle	SPAD, speckle
0.2	1229	1.425	6.050	7.445	5.323	32.877	31.580	3.382	2.313
0.4	2450	2.773	11.949	10.856	7.988	35.964	36.931	4.823	3.434
0.6	3685	4.162	17.861	12.775	9.576	37.060	38.586	5.139	3.673
0.8	4890	5.547	23.951	14.267	11.179	37.656	40.082	6.079	4.300
1.0	6155	7.003	30.101	15.459	11.575	37.930	40.557	6.862	5.289

Contrast (lower is better)									
R	N	CCD	Blurred	Ideal, 20%	SPAD, 20%	Ideal, 1%	SPAD, 1%	Ideal, speckle	SPAD, speckle
0.2	1229	0.214	0.065	0.247	0.291	0.156	0.204	0.325	0.404
0.4	2450	0.191	0.084	0.207	0.230	0.167	0.178	0.241	0.329
0.6	3685	0.178	0.119	0.187	0.206	0.163	0.161	0.210	0.285
0.8	4890	0.164	0.135	0.174	0.185	0.161	0.169	0.182	0.241
1.0	6155	0.153	0.148	0.176	0.178	0.156	0.160	0.174	0.223

Table 3.3: Visibility for imaging the single stripe targets with an average of one photon per illumination spot. The meaning of the headings is the same as in Table 3.2.

Visibility (higher is better)									
R	N, 1%	CCD, 1%	Blurred, 1%	Ideal, 20%	SPAD, 20%	Ideal, 1%	SPAD, 1%	Ideal, speckle	SPAD, speckle
0.2	1229	-0.049	-0.164	7.445	5.323	12.368	7.766	7.060	5.889
0.4	2450	0.026	0.145	10.856	7.988	18.907	11.862	10.104	7.927
0.6	3685	0.089	0.409	12.775	9.576	21.690	13.595	11.978	9.782
0.8	4890	0.168	0.767	14.267	11.179	24.991	16.955	13.549	10.336
1.0	6155	0.214	0.928	15.459	11.575	26.510	18.916	14.772	12.345

Figures 3.12 and 3.13 illustrate images formed under the conventional spatially resolved “Blurred” conditions and the images formed by the “SPAD” for the stripes having reflectivities  $R = 1$  and  $R = 0.2$ , respectively. The much better visibility of the correlation images is largely due to the sparseness of the reflected photon stream, since for both the illumination patterns and the reflected photons are often both zero valued. The low photon flux does result in many weaker, spurious correlations all over the image rather than a more uniform background. The CCD images, on the other hand, are dominated by the read noise of the electronics, which is approximately one order of magnitude larger than the average photon flux per pixel for  $R = 1$ .

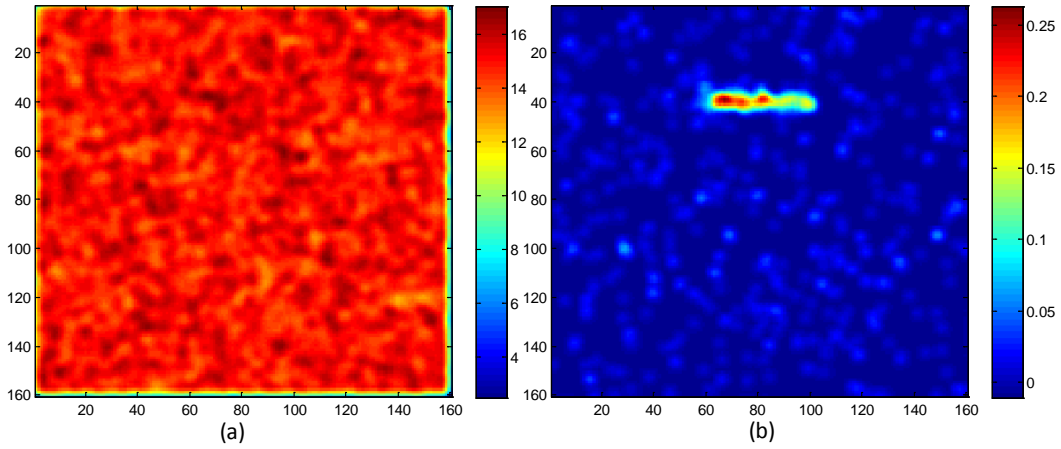


Figure 3.12: (a) “Blurred” CCD image and (b) correlation image of a stripe with  $R=1$ , illuminated with 10,000 realizations of the 1% coverage illumination having one photon per spot on average. The total number of photons reflected towards the detectors is 292.

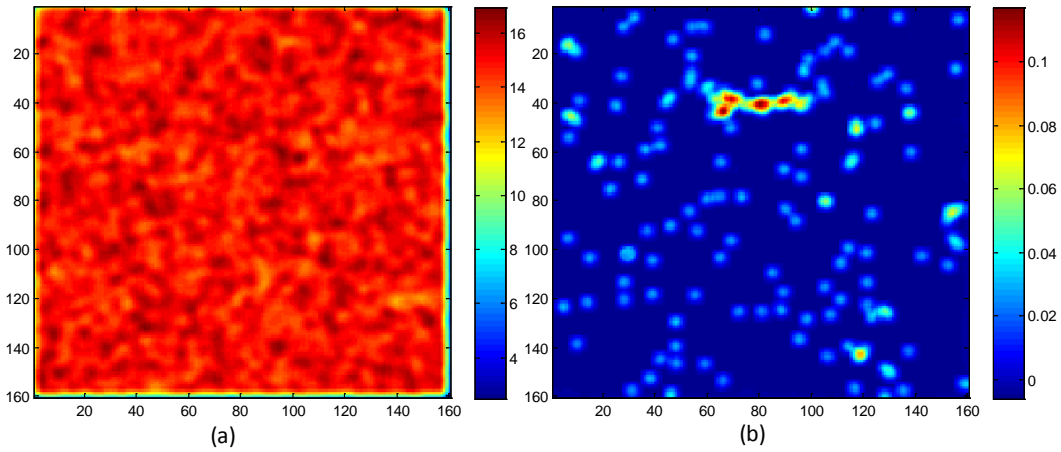


Figure 3.13: (a) “Blurred” CCD image and (b) correlation image of a stripe with  $R=0.2$ , illuminated with 10,000 realizations of the 1% coverage illumination having one photon per spot on average. The total number of photons reflected towards the detectors is 49.

Table 3.4: Visibility parameter when the random illumination has 20% coverage and an average of one photon per spot. The number of stripes in the target is either 1 or 5 as indicated.

Visibility (higher is better)								
R	CCD,1	CCD, 5	Blurred,1	Blurred, 5	Ideal, 1	Ideal, 5	SPAD, 1	SPAD ,5
0.2	1.454	1.435	6.2209	6.434	7.445	2.363	5.323	1.800
0.4	2.886	2.995	12.584	12.534	10.856	4.101	7.988	3.168
0.6	4.243	4.496	18.360	19.516	12.775	5.759	9.576	4.298
0.8	5.691	5.957	24.913	25.453	14.267	8.187	11.179	6.033
1.0	7.277	7.236	31.405	31.251	15.459	9.205	11.575	6.762

Based on the results of our numerical experiments, correlation imaging seems to offer attractive properties in low brightness imaging situations; however, it does have some unusual features. The first particularity is that the visibility of a correlation image is dependent on the area of the target as opposed to traditional spatially resolved imaging procedures. This is evident from the data shown in Table 3.4. When imaging all five stripes at the same time, the visibility of each of the stripes in the correlation image decreases noticeably. This is due to the increased number of random processes that contribute to the integrated signal, making the integrated intensity less correlated with any given process.

The second feature specific to CI at low light levels is that the calculated correlations become non-linear with respect to the target reflectivity as shown in Figure 3.14. The mean intensity of the stripes in the CCD images always changes linearly with the number of detected photons, but at low light levels the stripes become very difficult to distinguish from the background. Also, the fixed read noise causes the slope of the CCD's response to vary with the number of photons in the image.



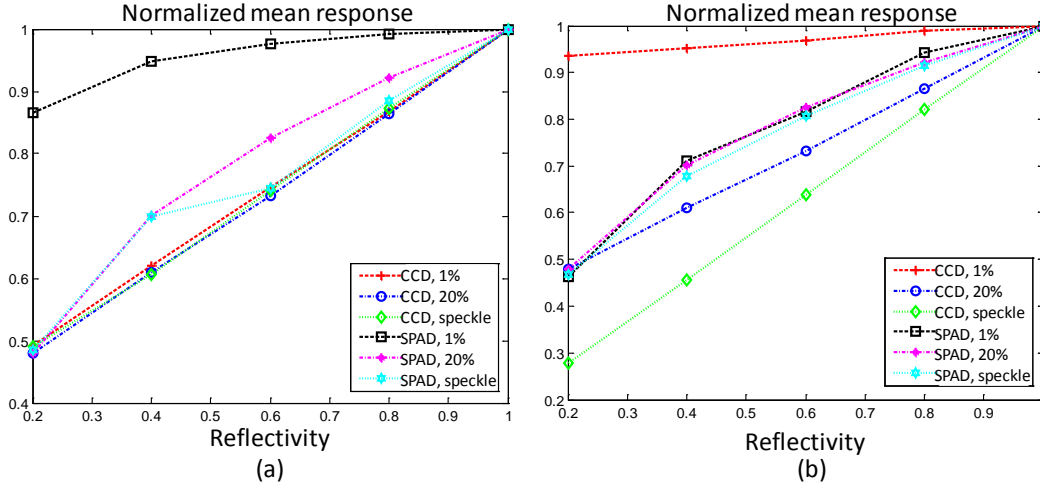


Figure 3.14: Plot of the mean value for each stripe as seen in the CCD and CI images for the three illumination conditions, normalized to the mean for the  $R = 1$  stripe, when (a) the total number of photons in the image and (b) the number of photons per speckle are constant. In (a) the CCD output changes very similarly under the three illumination conditions, but CI result becomes nonlinear as the number of speckles per pattern decreases. In (b), the correlation changes similarly for each type of illumination, but the CCD, while still linear, varies depending on the total photon flux because of the fixed level of the read noise. The lines only serve as guides.

To summarize, there are experimental circumstances in which correlation imaging may perform better than conventional spatially resolved imaging techniques. Specifically, it would be interesting to explore the CI approach for imaging weakly reflecting samples, as indicated by the high visibilities values, more than two orders of magnitude larger than the CCD visibilities, shown in Table 3.3. To that end, we are implementing a CI microscope. The set-up of the microscope is shown in Figure 3.15. A spatial light modulator is used to impose a spatially varying polarization onto a laser beam which is converted to an intensity modulation by a polarizer. Relay optics are used to image the SLM onto the back focal plane of a 60x microscope objective. The magnification of the SLM on the sample is controlled by adjusting this relay system. Figure 3.16 shows some preliminary data obtained using the experimental system. The

target is a microscope calibration slide with  $2\mu\text{m}$  wide stripes that have a center-to-center spacing of  $10\mu\text{m}$ . The illumination patterns have a spot size in the sample plane of approximately  $2\mu\text{m}$  and 5% coverage.

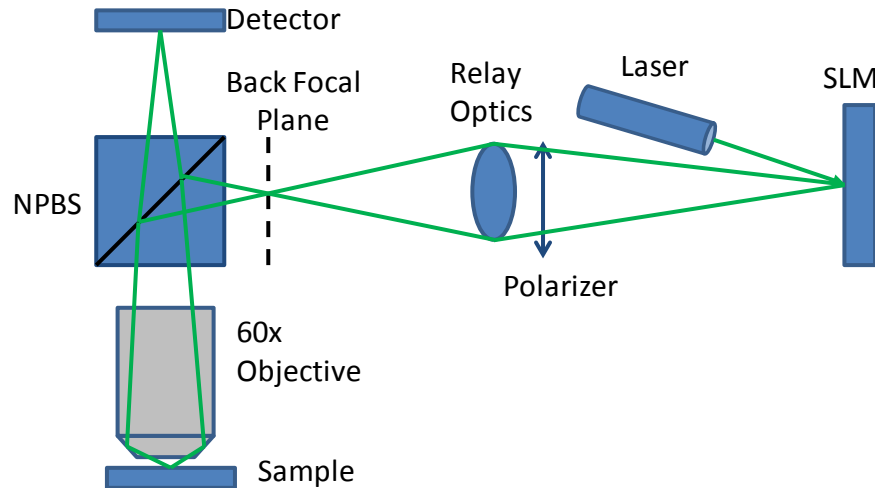


Figure 3.15: Schematic of a CI microscope. The SLM is used to create a spatially varying polarization state on the laser beam, and a polarizer is used to turn the polarization into a spatially varying intensity pattern. The intensity pattern is projected onto a sample through a microscope objective, and the reflected light is either imaged onto a CCD or integrated on a photodiode.

The ability of CI to form reasonable images with much higher visibility than CCD images at low light levels suggests that correlation imaging may be especially beneficial for examining media of biological origin which have notoriously weak reflectivities. This could enable label-free imaging of biological targets without the use of dyes, external markers, or the need for high photon fluxes. In the context of fluorescent microscopy, being able to image with low photon fluxes can help reduce the effects of photobleaching and phototoxicity in time series measurements [52]. Successful implementation of CI microscopy can therefore open new possibilities for real-time, in-vivo, and non-invasive examination of biological processes at cellular levels.

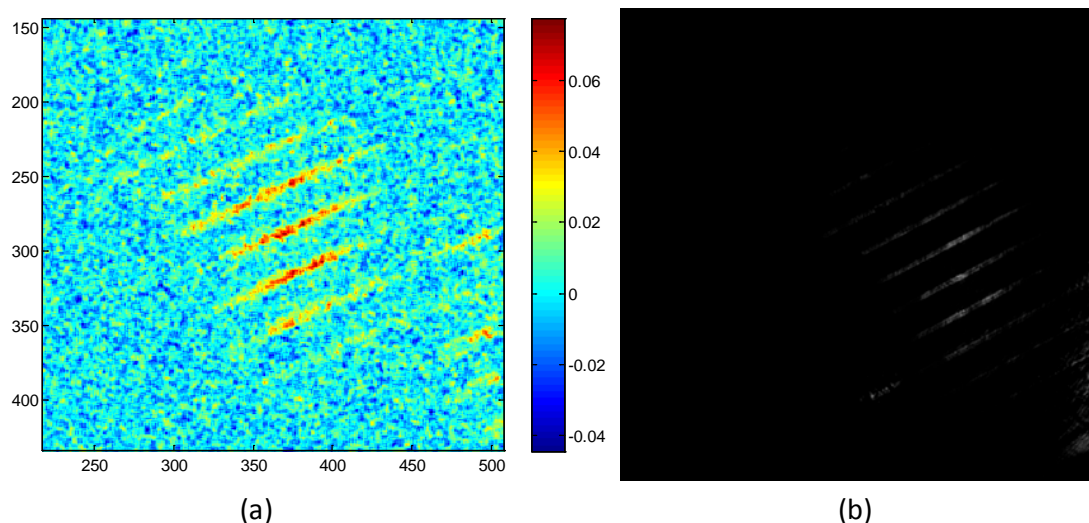


Figure 3.16: (a) Correlation image and (b) standard CCD image taken of a microscope calibration target. The stripes are approximately  $2\mu\text{m}$  wide and spaced by  $10\mu\text{m}$ . The size of the illumination spots in the target plane are approximately  $2\mu\text{m}$ .

## CHAPTER 4: OUTPUT FIELD MANIPULATION

The TM of a material can be directly measured; knowledge of the transfer function allows the input light to be structured such that, in combination with the medium, desirable net effects, such as focusing, can be produced. There are two primary methods for measuring the TM: searching for the TM via a brute force manipulation of an input wavefront and field measurements of the transmitted light. Both techniques will be discussed as well as some of their experimental demonstrations.

### 4.1 Searching for Transfer Matrices

If the TM associated with a scattering medium does not vary temporally, then each input field corresponds to a particular output field. The most direct way to produce a particular output is first solve the inverse problem to find the corresponding input, and then illuminate the medium with that input. Of course, solving the inverse problem using Maxwell's equations requires extensive and usually unavailable knowledge of the random medium. Alternatively, the inverse problem can be solved experimentally. One method of doing so is called phase conjugation. The desired output is created using sources, and the field that is transmitted from the sources to the other side of the medium is recorded. Once the transmitted field is recorded, it can be phase conjugated and sent back through the medium to produce the desired output, i.e. the one which had been initially created with sources. This technique is useful in radio frequency communication systems where the amplitude and phase of a field can be readily measured and will be discussed in more detail in Section 4.2.

In the optical regime, phase conjugation of a known wavefront can now be accomplished without too much difficulty using a spatial light modulator (SLM), but measuring a wavefront still requires an interferometric set-up. Sometimes, however, introducing a reference field may not be possible and an empirical approach is necessary. For instance, an algorithm for efficiently searching the input space to find an input that produces the desired output has recently been demonstrated by constantly measuring the output and using it as a feedback to drive the search as depicted in Figure 4.1 [2].

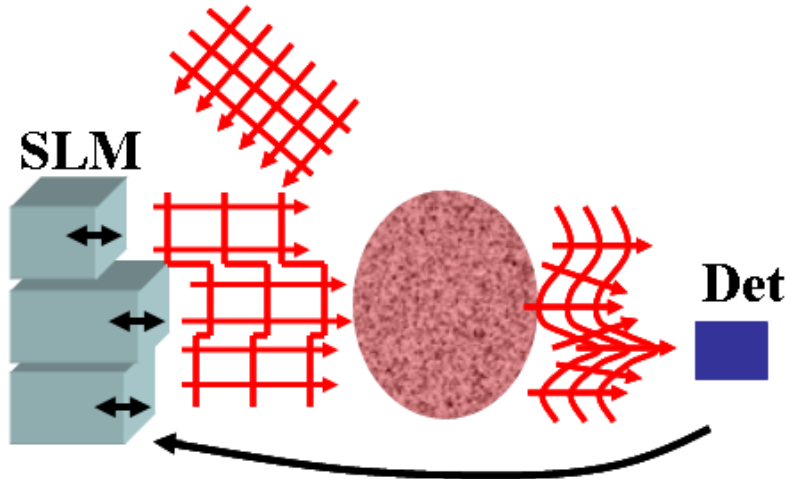


Figure 4.1: An output can be chosen by varying the input field and having a detector report the output. A blind search where the feedback is only used to determine if the desired output has been produced could take a significant amount of time to complete, but if the feedback is used intelligently, the search time can be decreased dramatically.

The basis of the technique is that the phases of the scattered waves in Equation 2.1 have two contributions: one from the material, which is constant, and another from the incident wavefront, which can be controlled to cause constructive interference with the other scattered waves, as shown below.

$$\vec{E}(\mathbf{r}, \omega) = \int a(\mathbf{r}, \mathbf{r}', \omega) E_{inc}(\mathbf{r}', \omega) \exp[\phi(\mathbf{r}, \mathbf{r}', \omega) + \psi(\mathbf{r}', \omega)] d\mathbf{r}', \quad (4.1)$$

where  $a(\mathbf{r}, \mathbf{r}', \omega) \exp[\phi(\mathbf{r}, \mathbf{r}', \omega)]$  transfers the input field incident at  $\mathbf{r}'$  to  $\mathbf{r}$  and  $E_{inc}(\mathbf{r}', \omega) \exp[\psi(\mathbf{r}', \omega)]$  is the incident field at  $\mathbf{r}'$ . Figure 4.2 show the idea schematically.

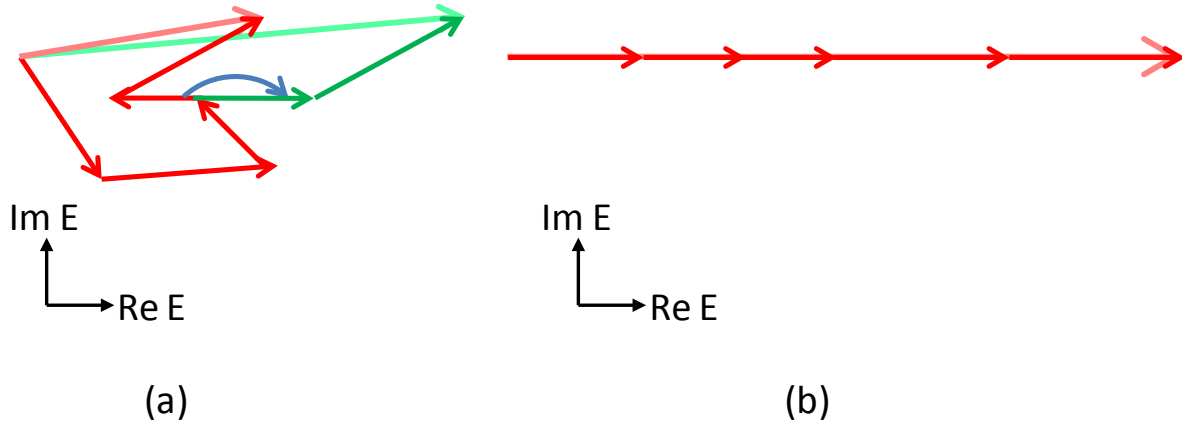


Figure 4.2: Bases of focusing via random media. (a) Scalar field in the output plane is the result of contributions from each input point. The phase of each contribution can be controlled to maximize the resulting summation as indicated in green. (b) Field after manipulating the incident wavefront.

Figure 4.2(a) shows the field at some point in the plane where the scattered field is to be controlled. It is made up of contributions from each point on the input side of the medium. The contributions each gain a net phase,  $\phi$ , by propagating through the medium and sum to yield a field with properties described in Section 4.2. However, if the phase of a given section of the input wavefront,  $\psi$ , is adjusted through  $2\pi$ , that section's contribution to the sum rotates through  $2\pi$  as well. Because there are very many input points  $\mathbf{r}'$  contributing to the resulting field, changes to one specific contribution will not appreciably affect the resultant; therefore, the phase of a particular section can be changed to cause that section's contribution to the scattered field to align with the original resultant vector. If the maximum (or minimum) of the resultant can accurately be determined as the phase of one section of the input is

changed, then the input contributions can be sequentially aligned with the original resultant field, as shown in Figure 4.2(b), thereby greatly increasing the intensity at that point compared to the intensity generated by a plane wave. Conceptually, they search the space of input wavefronts to find one for which the random medium's TM yields the desired output.

To verify this idea, a spatial light modulator was used to control the wavefront of a He-Ne laser beam. The modified wavefront was then passed through a scattering sample, and the resulting speckle pattern was recorded with a camera. The experimental set-up used is shown in Figure 4.3. The camera image was used in a feedback loop to monitor the intensity at one point and drive the SLM to maximize the intensity [2].

Focusing of light into five points arranged at the corners of a pentagon was also demonstrated. The achieved enhancement of the intensity at the focus spot that varied between 60 and 1000 times the average background before optimization. The large variation was attributed to the differing temporal stabilities of the scattering samples that used; also, the enhancement was a linear function of the number of regions used to shape the wavefront [2].

In an extension to the focusing work, light was focused onto a fluorophore embedded in a scattering medium [53]. The fluorophore was obscured by up to  $32\ \mu\text{m}$  of ZnO pigment and could not be detected visually. In the new geometry, the shaped wavefront focused the incident light onto the fluorophore, and the fluorescence signal was used to drive the feedback loop. For the case of a single fluorophore, the technique works well and achieved enhancements of the fluorescence signal of approximately 20 relative to the unoptimized case. In addition, the location of the fluorophore did not need to be known. Subsequently, this

experiment formed the basis of proposed microscopy [54] and endoscopy [55,56] techniques. Recently, several groups demonstrated almost simultaneously that pulsed light could be focused in time as well as space by finding the appropriate wavefront [57–59].

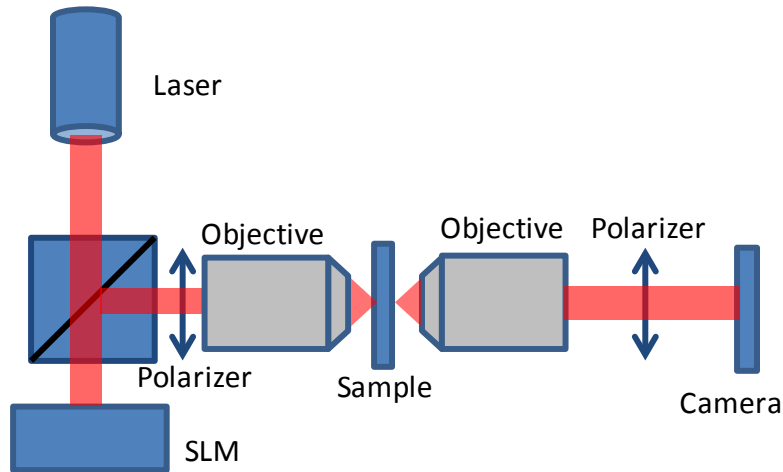


Figure 4.3: Set-up for controlling the field generated by scattering from a random medium.

Because the work presented in [2,53] finds the appropriate incident wavefront to create a desired intensity pattern after propagating through the scattering medium rather than measuring the TM of the medium directly, the search must be performed for each desired output. While a number of schemes to increase the speed of the search have been proposed [60], the ability to generate new patterns on the fly will always be hampered by the need to perform the search. In an extension to the work in [2] by another group, portions of an SLM have been used as a reference wave to determine the TM of a disordered sample rather than searching for the input wavefront that will correspond to a desired output [3]. The procedure of scanning the phase of one part of the SLM at a time is the same; however, the measured speckle patterns are then considered to be the interference of the reference portion



of the SLM with the controlled portion after propagation through the medium. Once the transfer is known, the desired output is decomposed into a combination of the measured outputs, for which the corresponding inputs are known. Light can be focused into arbitrary patterns by constructing an input wavefront from the wavefronts used to measure the TM, so no additional measurements are needed. Imaging a sparse scene through a diffusive random medium was also experimentally demonstrated [3]. Subsequently, the same group demonstrated the transmission of complex scenes through a random material as well [61]. Interestingly, imaging based on scattered intensity from a random object was shown experimentally with good results several years ago, although the object to be imaged had to be present during the calibration [62]. The work presented in [2] has also become the basis of a proposed endoscopic technique [63].

Imaging was shown to be theoretically possible, though technically very challenging, using intensity correlations nearly twenty years ago [64–67]. While [3] and [61] did not accomplished imaging directly through the correlation of speckle patterns, their focusing and imaging demonstrations have the same, rather severe, limitations. Imaging through a disordered material requires a large number of reference speckle patterns and has a limited depth of field. The imaged wavefront will be the one in the same plane as the reference speckle patterns, so if the object is not actually in that plane sharp imaging will not be possible. Also, the scattering medium must be quite stable because the reference speckle patterns are an interference phenomenon; even small reconfigurations of the scattering medium will cause speckle patterns of the same object taken before and after the reconfiguration to be

uncorrelated with one another. From the theory of DWS, the characteristic decorrelation time of the medium is proportional to  $(l^*/L)^2$ , where  $L$  is the thickness of the medium and  $l^*$  is the scattering mean free path [18].

#### 4.2 Measuring Transfer Matrices

We have already discussed TM measurements in the optical regime at the end of the previous section. The primary difference between measuring a TM and searching for an input that, after being acted on an unknown TM, produces the desired output is that when the TM is measured, new outputs can be generated without additional measurements. While imaging and focusing with random materials have only recently been demonstrated in the optical regime, they have been done for quite some time in the radio frequency regime and acoustics. The basic problem, shown below in Figure 4.4, is that a set of transmitters and a set of receivers are separated by or embedded in a multiply scattering medium; this geometry is known as multiple-input multiple-output (MIMO) in the communication field.

In a homogeneous medium, the transmitters are able to send out phase shifted copies of a signal that will interfere constructively in a certain direction, allowing them to focus their power towards the receivers. Similarly, the receivers can combine the detected signals with phase shifts to selectively measure in a certain direction [68]. With a scattering medium between them, if the transmitters try to transmit a signal to the receivers in the same way they would if the medium were not present, the multiple scattering would spread the signal in time and diffuse the power through out space.

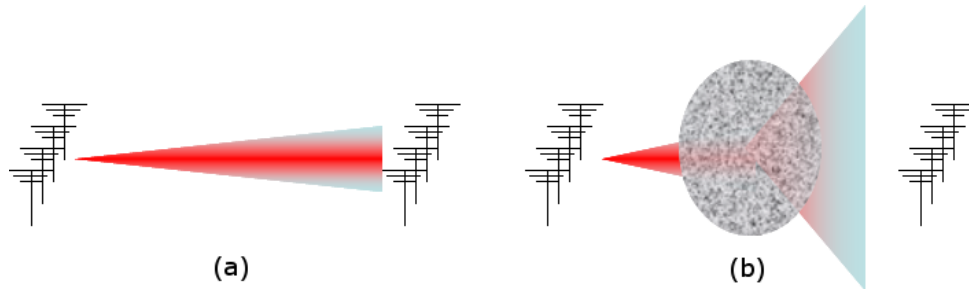


Figure 4.4: An array of transmitters and an array of receivers separated by a homogeneous material (a) or a randomly scattering material (b). In the homogeneous case, the transmitters are able to focus their power onto the receivers, but the scattering medium dissipates their power.

By knowing the TM of the random material, however, the transmitters can again work as they did in free space. The receivers sequentially emit a short pulse while the antennas record the multiply scattered field as shown in Figure 4.5(a). The recorded field gives the transfer function associated with the material for that input, in this case, the Green's function of propagation. Once the transmitters have these training fields, they can emit phase conjugated waveforms that will focus on to the receivers after propagation through the medium as depicted in Figure 4.5(b), thus allowing them to direct their energy towards the receivers once again [69–71].

Phase conjugation allows for more than simply transmitting as though the medium were not there; the multiply scattering medium can actually enhance the ability of the antennas to transmit data to the receivers using phase conjugation [68,72–74]. In a homogeneous medium, multiple transmitters can direct a signal towards a receiver, but, neglecting phase delays, all of the receivers measure the same signal. Thus, if the transmitters tried to combine multiple signals, the receivers would not be able to separate them; in the language of linear algebra, the receivers would have one equation with multiple unknowns. The scattering medium, on the

other hand, allows groups of transmitters to send multiple signals, one to each receiver, simultaneously. Because the training fields that focus on to each receiver individually are known, the transmitters simply need to emit the phase conjugate of the sum of the appropriate training fields. After propagating through the medium, each component of the input summation will focus onto its respective receiver. In effect, the scattering medium acts like a group of independent communication channels and enhances the capacity of the communication system [68–75].

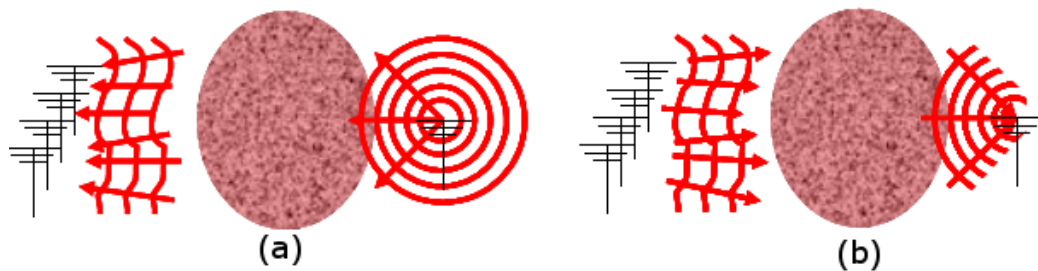


Figure 4.5: (a) An antenna sends a pulse through a scattering medium while other antennas record the scattered field. (b) The recording antennas send the phase conjugate of the previously recorded pulse back through the medium. After propagating through the medium, the signal focuses onto the original antenna.

## CHAPTER 5: INPUT FIELD CHARACTERIZATION USING MEASURED TRANSFER MATRICES

We have seen how the TM allows us to manipulate the light scattered from a random material, and the work in [3] has shown that imaging through a random material, or in other words determining the incident wavefront, is possible if the TM of the material is known as a function of the wavefront. The TM can be used to quantify many other properties of the light as well.

### 5.1 Polarimetry

While imaging an object through a scattering medium may be difficult, there are other applications, such as polarimetry, that do not require a large number of reference speckle patterns because the quantity of interest has fewer degrees of freedom. Much as the imaging idea relied on measuring the response of the random medium to "point" sources and then viewing the object as a collection of such sources, polarimetry requires measuring the response of the medium to different states of polarization and then decomposing an unknown state into the reference states.

Measuring the state of polarization of an unknown field was first demonstrated by correlating the speckle pattern produced by the unknown field with several reference speckle patterns [5]. The correlation of the unknown field's speckle pattern with the reference patterns in effect gives the contribution of each of the reference states to the unknown. However, since the scattered intensities, not the fields, are correlated, the speckle patterns need to be fully

developed in order to relate the intensity correlations to the field correlations via the Siegert relation.

Recently, polarimetry has been demonstrated by measuring the transfer functions of a randomly scattering material, instead of through correlations [4]. The transfer method demonstration does not require any special assumptions about the nature of the random field, meaning that it is valid even for partially developed random fields. Also, since spatial correlations are not used, the new demonstration is capable of quantifying spatially varying input fields [76].

The motivation for a TM based polarimeter is the same as the wavefront shaping experiment; the field at a given point after the scattering medium is a sum of many scattered contributions from the front side of the medium with appropriate scalings and rephasings; however, in this case the input field is a vector field.

To see more fully how the technique works, consider a slab scattering material illuminated by an arbitrary, monochromatic wave front with a uniform state of polarization at each point with nonzero intensity, as depicted in Figure 5.1. Locations on the input face of the slab are denoted by  $\mathbf{x}_i$ , and locations through out the volume where the scattered fields can reach are denoted by  $\mathbf{r}_i$ .

Let  $T_i(\mathbf{r}_j, \mathbf{x}_k)$  be the transfer of the field incident on the point  $\mathbf{x}_k$  to the point  $\mathbf{r}_j$  along scattering path  $i$ , then the total field at the detector,  $\mathbf{r}_{det}$  is obtained by adding the contributions of all scattering paths through the medium which end at the detector.

$$\vec{E}_{tot}(\mathbf{r}_{det}) = \sum_n \sum_j T_j(\mathbf{r}_{det}, \mathbf{x}_n) \vec{E}_{inc}(\mathbf{x}_n) \quad (5.1)$$

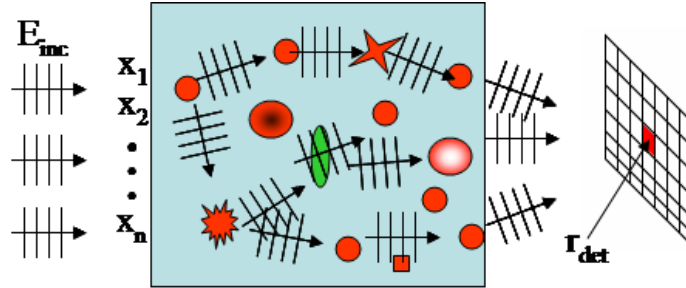


Figure 5.1: Light scattering inside a random slab.

If the polarization of the incident field is uniform across the face of the slab then a polarization unit vector can be factored out of the sums. In factoring out a polarization unit vector, we are not quite factorizing the scattering process because we leave the intensity distribution of the incident field with the description of the scattering.

$$\vec{E}_{tot}(\mathbf{r}_{det}) = \alpha(\mathbf{r}_{det}) \mathbf{e}_{inc} \quad (5.2)$$

Equation 5.2 makes it clear that the medium is essentially functioning as a spatially varying polarization transformation for the incident polarization state. If the matrix  $\alpha(\mathbf{r})$  can be determined, then by combining the measurements performed at several different locations, the incident Stokes' vector can be estimated. A brief examination of  $\alpha(\mathbf{r})$  shows that not all of the elements of the matrix are needed because the output field contains complete information about the incident field in both of its components. Therefore, by measuring the scattered light through a polarizer and neglecting the global phase, the remaining elements of  $\alpha(\mathbf{r})$  can be measured at each point in the output plane using standard techniques used to calibrate Stokes polarimeters [4].

Because we can easily measure intensities rather than fields, Equation 5.2 is more useful when expressed as intensities but also more cumbersome to work with. Fortunately, because the scattering medium, and therefore the interferences inside it, is fixed, we can work directly with the measured intensities. The measurement of a Stokes vector,  $\mathbf{S}$ , can be ideally depicted as  $\mathbf{I} = \mathbf{M} \cdot \mathbf{S}$ , where  $\mathbf{I}$  represents the column vector of intensity measurements from each of the speckles being used in the analysis.  $\mathbf{M}$  is the measurement matrix of the polarimeter and is determined by  $\alpha$  by viewing  $\alpha$  as a combination of waveplates and polarizers. Each row of  $\mathbf{M}$  is the first row of the Mueller matrix for the corresponding speckle, so it couples the polarization state into the measured intensity.

If each speckle used in the analysis samples the input field differently, then  $\mathbf{M}$  is invertible, and the incident Stokes vector can be estimated as

$$\mathbf{S} = \mathbf{M}^{-1} \cdot \mathbf{I}. \quad (5.3)$$

If more than four different speckles are used, the TM is not invertible because the system is overdetermined, i.e., it has more rows than columns, and a pseudoinverse of  $\overline{\mathbf{M}}$  must be used instead. Noise in the measurements will result in the measurements being inconsistent, so the least squares solution for the Stokes vector, given by the Morse-Penrose pseudoinverse, is usually found.

There are a few interesting points to be noted about this type of polarization measurement. First, because  $\alpha(\mathbf{r})$ , or equivalently  $\overline{\mathbf{M}}$ , essentially represents a mapping between the incident and the measurement coordinate systems, see Figure 5.2, the orientation of the measurement polarizer does not matter; the orientation of the measurement system is



given by the calibration states rather than the orientation of the measurement system. Second, because the spatial distribution of amplitude and phase only factors out of Equation 5.2 for a uniform distribution, simple calibration schemes will require that the field to be measured and the calibration field have the same intensity distribution and wavefront to be valid. If either the intensity or phase distributions vary, the contributions of the scattering paths to the final field will not be the same for the calibration fields and the field to be measured; in effect, the unknown field will interact with a different realization of the scattering material than the calibration fields.

An example of data collected with this kind of a system is shown in Figure 5.3. The illumination was a uniform state of polarization with an expected Stokes vector of  $(Q,U,V) = (0.577,-0.577,-0.577)$ . In the figure, each of the blue dots is a calculation of the incident state using 40 speckles as a single, overdetermined polarimeter. Because there is no reason to form any particular group of speckles into a polarimeter, many different groups can be formed and the polarization analysis repeated many times. The geometric center of the cloud of white points is shown as a white dot located at  $(Q,U,V) = (0.62,-0.59,-0.52)$ .

Equation 5.1 seems to imply that random materials can only analyze uniform polarization states because of the interferences in the medium; however, the geometry shown in Figure 5.2 is capable of measuring fields with a spatially varying state of polarization [76]. Essentially, the random medium is a thin layer of scatterers covering an imaging fiber bundle that encode the polarization state into intensity scattered into the fibers. The thin layer of scattering material covering the input face of the fiber bundle ensures minimal spreading of the

local incident polarization over the fiber face, and the waveguide structure minimizes cross talk during propagation to the detection electronics. Groups of neighboring fibers can be used to perform a local polarization analysis.

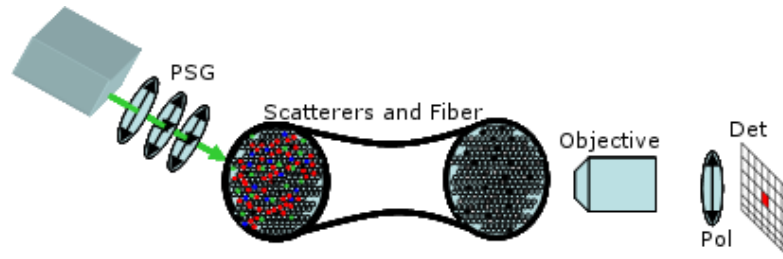


Figure 5.2: Geometry of a spatially resolved TM based polarimeter. A thin layer of scattering material is applied to the face of an imaging fiber bundle to allow access to local states of polarization.

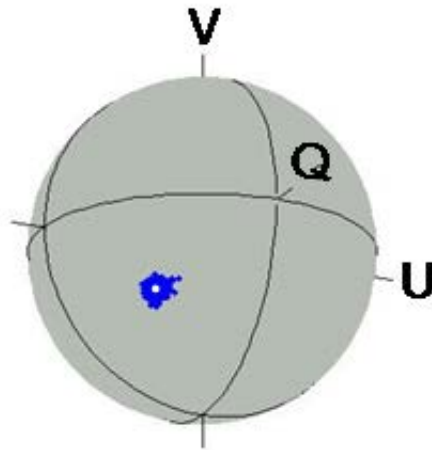


Figure 5.3: Example data collected with TM based polarimetry concept.

To test the performance of the polarimeter with a scene containing rapid variation in the polarization state, a checker pattern with sharp changes in polarization state at the edges of the checkers was imposed on an input beam. The U component of the Stokes vector measured for the checker pattern is shown in Figure 5.4. The white box in Figure 5.4(b) shows the approximate area measured by the fiber polarimeter,  $148 \times 163 \mu m$ . The Q component is 0 and

nearly uniform, the V component is not uniform but is the inverse of the U component and looks very similar to the images shown. The main features of the checker pattern are recovered by the fiber polarimeter, but the impact of spatial averaging is also present due to the rapid variation of the polarization state. This image was performed using groups of four fibers selected from an 18  $\mu m$  diameter circle centered on the location of the shown data. The extent of spatial averaging could be controlled by adjusting the size of the measurement area during processing until only the four closest elements in the area are included in the sampling area.

Due to the large number of speckles available for analysis, this technique offers many different adjustable parameters in the analysis: the number and orientations of the analyzers (i.e. speckles) in each polarimeter, the method of analysis used (data reduction matrix, Fourier transform, etc), and the spatial resolution used to analyze the unknown field.

Performing polarimetry with random scattering carries a few important restrictions. Although traditional polarization optics are not needed for the measurement, the wavefronts of the unknown and the reference fields must be the same for the speckle patterns to be correlated. Also, the scattering medium must be mechanically stable for both the calibration and measurement.

Implementing a polarimeter using a scattering material followed by a wave guide offers several desirable features. The spatial resolution is comparable to traditional polarimetric techniques; however, the resolution of this method can be traded off with the measurement precision to optimize the analysis of the unknown field in post processing. Figure 5.5 shows the

data from Figure 5.3 processed using 4, 8, 24, and 40 speckles as a single polarimeter. The average state recovered does not shift, but the spread of the recovered states decreases dramatically. Also, the wavelength to be analyzed is chosen by the calibration wavelength, so examining sources of various colors does not require any adjustments to the measurement device itself. The working wavelength range of the device is determined by the spectral response of the fiber bundle and detector, which is very broad compared to traditional polarization optics. The parallel nature of the measurement means that its temporal resolution can be quite high. Finally, the polarimeter performs a full polarization analysis with a probe that is very simple and compact. We expect the concept to find applications in microscopy, endoscopy [5], and any other area where simultaneous sampling of many points is required.

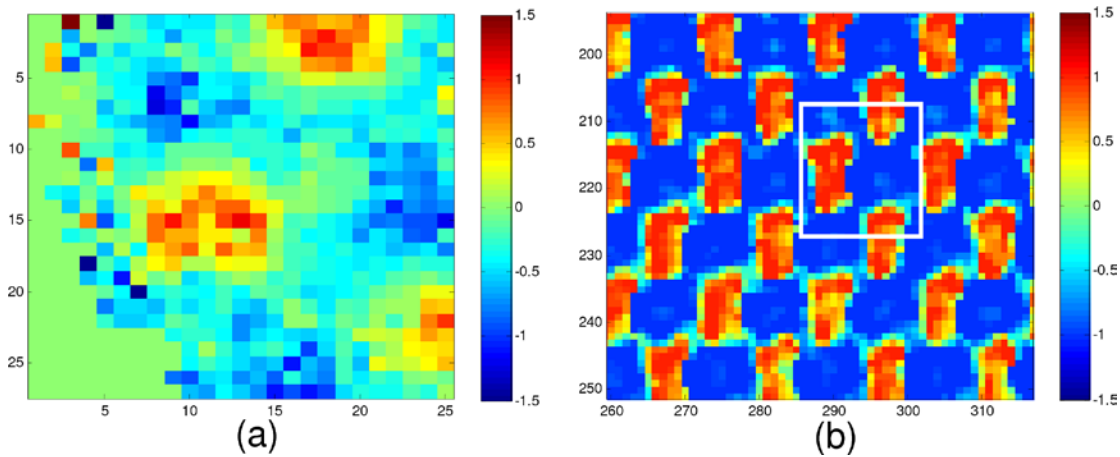


Figure 5.4: The U component of the Stokes vector for a checker pattern generated by a SLM. (a) The measurement made by the fiber polarimeter. (b) The measurement made using a polarizer and CCD array. The white box indicates the approximate area measured by the fiber polarimeter.

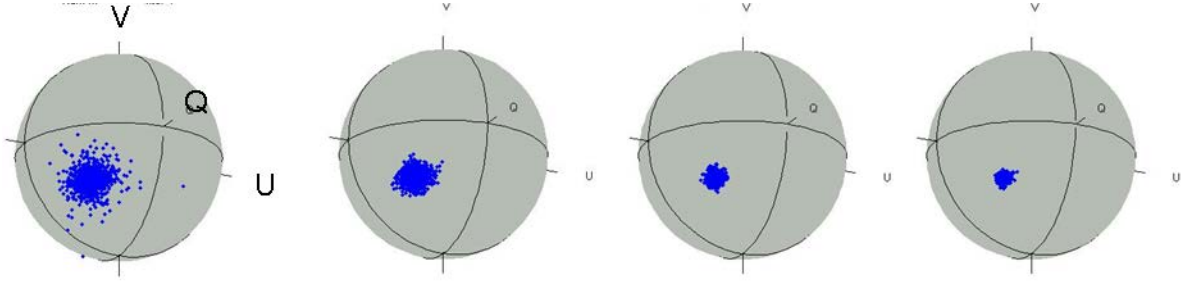


Figure 5.5: Polarimetric data processed using groups of 4, 8, 24, and 40 speckles per polarimeter.

## 5.2 Spectroscopy

Another application of the transfer matrix method is for spectral measurements. The spectral transmission of the random material will vary across the face of the material because speckle patterns generated by different wavelengths will be uncorrelated with one another. Using a tunable source, the spectral transmission at each detector location can be measured. The total field will be of the form

$$E_{tot}(\mathbf{r}) = \iint a(\mathbf{r}, \mathbf{r}', \omega) E_{in}(\mathbf{r}', \omega) d\mathbf{r}' d\omega. \quad (5.4)$$

As with the polarization measurement, if the spectrum is uniform across the input, a spectral vector can be factored out of the spatial integral. When the material is exposed to the unknown spectrum, the random material will sample the spectrum in many different ways and the resulting intensity of each sampling will be recorded. The unknown spectrum can be calculated by solving a system of linear equations using a spectral calibration of the medium [6].

We have demonstrated that spectrally resolved polarimetric information can be measured using the TM of a disordered material [77]. Some spectra measured from the scattered produced by a random material and a traditional spectrometer are shown in Figure 5.6. Because of the finite number of calibration spectra that can be used in a real experiment,

the integral in Equation 5.4 is approximated with a sum; the TM used for the measurement shown in Figure 5.6 was measured every 3nm. As can be seen, the measured spectra agree quite well with one another. The polarimetric aspect of the measurement was similar to the results already shown.

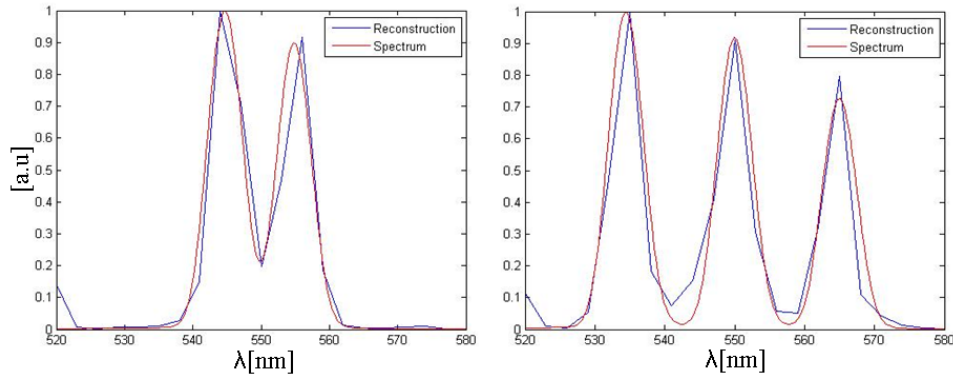


Figure 5.6: Some example spectra measured using a conventional spectrometer (red line) and a random material (blue line).

Naturally, the spectral measurement can be extended to measure spatially varying spectra in the same manner as in [3]. We demonstrated this concept using an LCD monitor, imaged onto the system shown in Figure 5.2, as a source of spatially varying spectra. Calibration data were taken for the red and green outputs of the monitor, and then a pattern of red and green stripes was displayed on the monitor. A representative set of data is shown in Figure 5.7.

Characterizing the input to a random system and controlling the output from the system both involve measuring the TM of the medium as a function of the parameter of the light to be measured or controlled. However, the number of elements of the TM that need to be measured vary considerably depending on the number of degrees of freedom in the input. For example, to measure an input spectrum, we have to measure one element of the material's TM for each component of the spectrum; however, for polarimetry, we only need to measure four,

well-chosen elements of the TM because any polarization state can be decomposed into those elements.

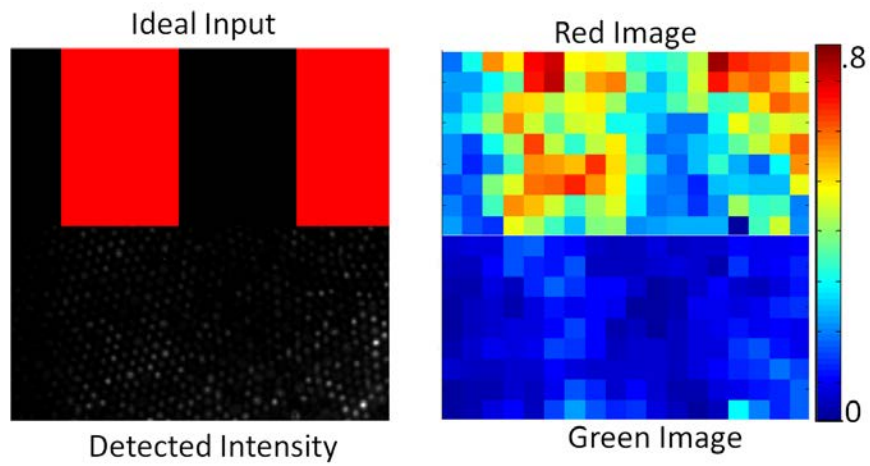


Figure 5.7: An example of a spatially varying spectrum measured using a random material.

## **CHAPTER 6: SUMMARY OF ORIGINAL CONTRIBUTIONS AND CONCLUSIONS**

Linear systems theory (LST) has been a powerful tool in the development of optics. In the view of LST, when an illumination field excites a material system, the interaction of the field with the medium deterministically produces an output field. The medium can then be characterized by a transfer matrix (TM) that connects the input and output fields. Three fundamental problems can be posed in LST: (i) the determination of the medium's properties based on knowledge of the inputs and outputs, (ii) the determination of the output's properties based on knowledge of the inputs and the medium, and (iii) the determination of the input's properties based on knowledge of the medium and the outputs.

While several topics in this dissertation were motivated by recent research related to the second LST problem, specifically controlling the output of a random scattering system, we have largely focused on the first and third questions.

In the case of random media, the first problem produced mixed results. It was shown in Chapter 2 that scattered fields with contributions from many independent scatterers have universal statistical properties, independent of the scattering medium. In some cases however, the scattered field does not develop universal statistics and can be used as a fingerprint for the medium, as discussed in Chapter 3. As a practical example, we sought to distinguish between asphalt samples that had been pressed with different pressures and in some cases had their surfaces obscured with sand or water. The samples were illuminated with a linearly polarized laser beam, and the distribution of backscattered polarization states was measured. Based on the



polarization statistics of the backscattered light, we showed that the asphalt samples could be distinguished from one another and that asphalt covered with sand or water could be distinguished from the unobscured asphalt.

Even in the case where the light scattered from the sample does have universal statistics, useful information about the scattering system may be contained in the dynamics of the scattered light. The field distribution that results from scattering depends on the specific realization of the scattering system; if the system is dynamic, the scattered field will have temporal as well as spatial fluctuations. We discussed two measurement techniques, dynamic light scattering and diffusive wave spectroscopy, that seek to relate the temporal autocorrelation of the light scattered from particles in suspensions to the diffusion coefficient of the scatterers.

In the course of studying fluctuating fields, such as those occurring in dynamic light scattering, we developed a new theory for determining the state of polarization of the scattered field from the intensity fluctuations of the scattered field mixed with a local oscillator as a function of the oscillator's state of polarization, and presented a proof of concept experiment utilizing the pseudothermal light created by rotating diffusers. This novel fluctuation polarimetry was also discussed in Chapter 3. As noted, the relationship between the degree of polarization (DOP) and the contrast of intensity fluctuations was discovered by generalizing the analysis of intensity interferometry to electromagnetic fields [31]. The demonstrated technique is advantageous in that it requires little change to current

measurement set-ups, does not discard any of the scattered light, and because of its interferometric nature, may be used to amplify the signal from weakly scattering systems.

Random fields also emerge from the interaction with material systems that are not intrinsically dynamic. For example, speckle interferometry techniques attempt to quantify local changes in the spatial distribution of the scattered light as a test object is slowly placed under a load. For small shifts, the local shifts in the scattered light can be related to local shifts in the test object.

Another approach to material determination considers probing the material with randomly fluctuating fields. This technique is utilized in aperture correlation microscopies (ACM) and correlation imaging (CI). The primary difference between ACM and CI is that the former records the scattered light using a spatially resolved detector whereas CI integrates the scattered light using a bucket detector. In CI, the image is then formed by correlating the integrated signal with the random illumination patterns. The correlation image yields the material's reflectivity or transmissivity, depending on the experimental geometry, because the correlation image essentially tells how much of the integrated signal is due to each portion of the random illumination. We studied in detail the quality of correlation images compared to traditional imaging. Typical CI techniques use fully developed speckle patterns to probe the medium, but by projecting the surface of an amplitude-only spatial light modulator onto the sample plane, we are able to create arbitrary random illuminations. For the random illumination patterns used to generate the correlation images, we examined typical fully developed speckle patterns as well as patterns generated by randomly generating illumination

spots with a Gaussian intensity profiles. In addition to considering the effects of different types of random illumination, we were able to account for the additional randomness due to the partitioning the photon stream caused by subunity target reflectivity and detector quantum efficiency. All these aspects are critical for situations characterized by low illumination levels, specific to biological microscopies, and have not been previously considered.

Our results demonstrate that, at low photon fluxes, the imaging characteristics of a correlation imager can be substantially better than that achieved with a standard CCD based imaging. The comprehensive critical analysis of these imaging modalities indicates that the performance of a spatially-resolved imager is essentially independent of the type of illumination but sensitive to the total number of photons. On the other hand, the quality of correlation imaging procedure depends on the total area of the target and the CI outcome can be controlled by the type illumination used. These findings were then used to design a multifunctional imaging setup for implementing correlation imaging strategies. Preliminary data obtained with this new type of correlation imaging microscope were also presented. This constitutes a testbed to experimentally validate the performance of different correlation imaging modalities, some of which were not discussed here.

The second LST problem, the direct calculation of the scattered field based on knowledge of the input and the medium, implies that knowing TM of a particular medium allows the selection specific outputs by controlling the input. Other researchers have demonstrated this idea by focusing light through a random material, which may have

applications in photodynamic therapies. Properties besides the output intensity distribution, such as the polarization states or spectrum, could also be controlled.

Motivated by the research on controlling the scattered light from a random medium, we investigated how knowledge of TM's allows one to infer properties of the input field based on the scattered light and discussed our results in Chapter 5. By their nature, random media produce many different samplings or mixings of the input field, but unlike more traditional optical elements, random materials sample all properties of the input field. As a result, disordered materials could be expected to be able to serve in place of many different types of traditional optical components or systems if the appropriate subsets of the TM were known or learned through a calibration procedure [66]. We have demonstrated that random materials may be calibrated both polarimetrically and spectropolarimetrically, and that they may be used to measure unknown fields. We have shown for the first time that in realistic situations a random medium can be used to perform spatially resolved measurements of the polarimetric and spectroscopic properties of an unknown field. Our experiments demonstrated a full Stokes polarimeter on the end of an imaging fiber bundle with a diameter of approximately 150 $\mu$ m and a spatial resolution of 18 $\mu$ m. Moreover, we have also demonstrated that spectroscopic measurements can be simultaneously performed using the same setup. Such spectropolarimetric measurements achieved a spectral resolution of 3nm over a 60nm band and 1.5nm over a 30nm band while simultaneously determining the Stokes vector of the incoming radiation.

Interestingly, the property of the input field that is estimated by a random material depends only on the subset of the TM that is used in the analysis, meaning that scattering from one realization of a material can reveal many different properties about the input by simply changing the calibration data used to analyze the measured data rather than changing the physical interaction. That is quite different from regular optical systems where the decision to measure a property of the field has to be made before the measurement is taken. It should be noted that the other properties of the unknown light must be the same as that of the calibration light. For example, it is possible to measure the spectral response of a material; however, the material may also have a polarimetric response. In that case, either a full spectropolarimetric measurement must be made or the polarimetric properties of the spectral calibration source must match those of the unknown source. With that caveat, the potential for adaptive measurements based on sampling performed by random media may have unique applications.

This dissertation covered several examples of measurements that use the properties of random fields rather than simply overcome the inherent fluctuations resulting from the interaction of optical fields with complex material systems. Some of the novel techniques described here may find use in challenging measurement scenarios involving weak light-matter interactions and low-light level scattering.

**APPENDIX:**  
**PUBLICATIONS AND PRESENTATIONS**

#### A. Refereed Papers

1. Thomas Kohlgraf-Owens and Aristide Dogariu, "Finding the field transfer matrix of scattering media," Opt. Express 16, 13225-13232 (2008).
2. Thomas Kohlgraf-Owens and Aristide Dogariu, "Spatially resolved scattering polarimeter," Opt. Lett. 34, 1321-1323 (2009).
3. Thomas W. Kohlgraf-Owens and Aristide Dogariu, "Transmission matrices of random media: means for spectral polarimetric measurements," Opt. Lett. 35, 2236-2238 (2010).
4. Thomas Kohlgraf-Owens and Aristide Dogariu, "Fluctuation polarimetry," Opt. Lett. 37, 1961-1963 (2012).
5. Thomas Kohlgraf-Owens and Aristide Dogariu, "Correlation imaging at low light levels," (in preparation).

## B. Oral Presentations

1. T. Kohlgraf-Owens and A. Dogariu, "Disordered media as efficient optical devices," in *Frontiers in Optics*, OSA Technical Digest (CD) (Optical Society of America, 2008), paper FWS4.
2. T. Kohlgraf-Owens and A. Dogariu, "Leveraging scattering for polarization analysis," in *SPIE Defense, Security, and Sensing 2009*, SPIE Technical Program (SPIE, 2009), presentation 7316-21.
3. T. Kohlgraf-Owens and A. Dogariu, "Optimized polarimetry with massively parallel polarization sampling," in *SPIE Optics+Photonics 2009*, SPIE Technical Program (SPIE, 2009), presentation 7461-31.
4. T. Kohlgraf-Owens and A. Dogariu, "Snapshot spectro-polarimetry using disordered materials," in *Computational Optical Sensing and Imaging*, OSA Technical Digest (CD) (Optical Society of America, 2009), paper CWA4.
5. K. M. Douglass, T. Kohlgraf-Owens, J. Ellis, C. Toma, A. Mahalanobis, and A. Dogariu, "Expanded field of view using polarization multiplexing," in *Computational Optical Sensing and Imaging*, OSA Technical Digest (CD) (Optical Society of America, 2009), paper CWA5.
6. T. Kohlgraf-Owens, A. Dogariu, D. Ma, and D. Carter, "Understanding the particle size/shape ambiguity and its impact on optical responses of particulate composites," in *2010 TAPPI Advanced Coating Fundamentals Symposium*, TAPPI Technical Digest (CD) (TAPPI, 2010), paper 4.2.
7. T. Kohlgraf-Owens and A. Dogariu, "Intensity fluctuation polarimetry," in *Frontiers in Optics*, OSA Technical Digest (Optical Society of America, 2011), paper FThV5.
8. T. Kohlgraf-Owens and A. Dogariu, "Imaging spectroscopy without a spectrometer," in *Frontiers in Optics*, OSA Technical Digest (Optical Society of America, 2011), paper FML3.



### C. Posters

1. T. Kohlgraf-Owens, J. Ellis, and A. Dogariu, "Scattering of three dimensional optical radiation," in *Frontiers in Optics*, OSA Technical Digest (CD) (Optical Society of America, 2006), poster JSuA32.

## LIST OF REFERENCES

1. J. Goodman, *Introduction to Fourier Optics*, 3rd ed. (Roberts & Co, 2005).
2. I. M. Vellekoop and A. P. Mosk, "Focusing coherent light through opaque strongly scattering media," *Opt. Lett.* **32**, 2309–2311 (2007).
3. S. M. Popoff, G. Lerosey, R. Carminati, M. Fink, A. C. Boccara, and S. Gigan, "Measuring the Transmission Matrix in Optics: An Approach to the Study and Control of Light Propagation in Disordered Media," *Physical Review Letters* **104**, 4 (2010).
4. T. Kohlgraf-Owens and A. Dogariu, "Finding the field transfer matrix of scattering media," *Opt. Express* **16**, 13225–13232 (2008).
5. I. Freund, "Stokes-vector reconstruction," *Optics Letters* **15**, 1425–1427 (1990).
6. Z. C. Xu, Z. L. Wang, M. E. Sullivan, D. J. Brady, S. H. Foulger, and A. Adibi, "Multimodal multiplex spectroscopy using photonic crystals," *Optics Express* **11**, 2126–2133 (2003).
7. J. Goodman, "Statistical Properties of Laser Speckle Patterns," in *Laser Speckle and Related Phenomena*, J. C. Dainty, ed. (Springer-Verlag, 1975).
8. J. Goodman, *Speckle Phenomena in Optics Theory and Applications* (Roberts & Co, 2007).
9. M. G. Bulmer, *Principles of Statistics*, 2nd ed. (Dover Publications, 1979).
10. P. Zakharov, F. Cardinaux, and F. Scheffold, "Multispeckle diffusing-wave spectroscopy with a single-mode detection scheme," *Physical Review E* **73**, 011413 (2006).
11. S. E. Skipetrov and R. Maynard, "Dynamic multiple scattering of light in multilayer turbid media," *Physics Letters A* **217**, 181–185 (1996).
12. I. Freund, M. Rosenbluh, and S. Feng, "Memory Effects in Propagation of Optical Waves through Disordered Media," *Physical Review Letters* **61**, 2328 (1988).
13. J. Ellis and A. Dogariu, "Discrimination of globally unpolarized fields through Stokes vector element correlations," *J. Opt. Soc. Am. A* **22**, 491–496 (2005).
14. R. Bandyopadhyay, A. S. Gittings, S. S. Suh, P. K. Dixon, and D. J. Durian, "Speckle-visibility spectroscopy: A tool to study time-varying dynamics," *Review of Scientific Instruments* **76**, 093110 (2005).
15. V. A. Bloomfield, "Biological Applications," in *Dynamic Light Scattering*, R. Pecora, ed. (Plenum Press, 1985).

16. B. J. Berne and R. Pecora, *Dynamic Light Scattering* (John Wiley & Sons, 1976).
17. D. J. Pine, D. A. Weitz, P. M. Chaikin, and E. Herbolzheimer, "Diffusing wave spectroscopy," *Physical Review Letters* **60**, 1134 (1988).
18. D. A. Weitz and et al, "Diffusing-wave spectroscopy: The technique and some applications," *Physica Scripta* **T49B**, 610 (1993).
19. G. Maret and P. E. Wolf, "Multiple light-scattering from disordered media - the effect of brownian-motion of scatterers," *Zeitschrift Fur Physik B-Condensed Matter* **65**, 409–413 (1987).
20. M. J. Stephen, "Temporal fluctuations in wave propagation in random media," *Physical Review B* **37**, 1 (1988).
21. F. Scheffold, S. E. Skipetrov, S. Romer, and P. Schurtenberger, "Diffusing-wave spectroscopy of nonergodic media," *Physical Review E* **63**, 061404 (2001).
22. D. J. Pine, D. A. Weitz, J. X. Zhu, and E. Herbolzheimer, "Diffusing-wave spectroscopy: dynamic light scattering in the multiple scattering limit," *J. Phys. France* **51**, 2101–2127 (1990).
23. G. Dietsche, M. Ninck, C. Ortolfo, J. Li, F. Jaillon, and T. Gisler, "Fiber-based multispeckle detection for time-resolved diffusing-wave spectroscopy: characterization and application to blood flow detection in deep tissue," *Appl. Opt.* **46**, 8506–8514 (2007).
24. J. G. Walker, P. C. Y. Chang, K. I. Hopcraft, and E. Mozaffari, "Independent particle size and shape estimation from polarization fluctuation spectroscopy," *Measurement Science and Technology* **15**, 771–776 (2004).
25. P. C. Y. Chang, K. I. Hopcraft, E. Jakeman, and J. G. Walker, "Optimum configuration for polarization photon correlation spectroscopy," *Measurement Science and Technology* **13**, 341–348 (2002).
26. M. C. Pitter, K. I. Hopcraft, E. Jakeman, and J. G. Walker, "Structure of polarization fluctuations and their relation to particle shape," *Journal of Quantitative Spectroscopy and Radiative Transfer* **63**, 433–444 (1999).
27. O. Kusmartseva and P. R. Smith, "Robust method for non-sphere detection by photon correlation between scattered polarization states," *Measurement Science and Technology* **13**, 336–340 (2002).

28. P. R. Smith, O. Kusmartseva, and R. Naimimohasses, "Evidence for particle-shape sensitivity in the correlation between polarization states of light scattering," *Opt. Lett.* **26**, 1289–1291 (2001).
29. D. Haefner, S. Sukhov, and A. Dogariu, "Stochastic Scattering Polarimetry," *Phys. Rev. Lett.* **100**, 043901 (2008).
30. S. Sukhov, D. Haefner, and A. Dogariu, "Stochastic sensing of relative anisotropic polarizabilities," *Phys. Rev. A* **77**, 043820 (2008).
31. E. Wolf, "Correlation between Photons in Partially Polarized Light Beams," *Proceedings of the Physical Society* **76**, 424–426 (1960).
32. L. Mandel and E. Wolf, *Optical Coherence and Quantum Optics* (Cambridge University Press, 1995).
33. T. Kohlgraf-Owens and A. Dogariu, "Fluctuation polarimetry," *Optics Letters* **37**, 1961–1963 (2012).
34. L. Mandel and E. Wolf, *Optical Coherence and Quantum Optics* (Cambridge UP, 1995).
35. E. Collett, *Polarized Light. Fundamentals and Applications* (Dekker, 1993).
36. P. K. Rastogi, ed., *Digital Speckle Pattern Interferometry and Related Techniques* (John Wiley & Sons, 2001).
37. S. Zhang, B. Hu, P. Sebbah, and A. Z. Genack, "Speckle evolution of diffusive and localized waves," *Physical Review Letters* **99**, 4 (2007).
38. T. Wilson, R. Juškaitis, M. A. A. Neil, and M. Kozubek, "Confocal microscopy by aperture correlation," *Opt. Lett.* **21**, 1879–1881 (1996).
39. S.-H. Jiang and J. G. Walker, "Speckle-illuminated fluorescence confocal microscopy, using a digital micro-mirror device," *Measurement Science and Technology* **20**, 065501 (2009).
40. C. Ventalon and J. Mertz, "Quasi-confocal fluorescence sectioning with dynamic speckle illumination," *Opt. Lett.* **30**, 3350–3352 (2005).
41. C. Ventalon and J. Mertz, "Dynamic speckle illumination microscopy with translated versus randomized speckle patterns," *Opt. Express* **14**, 7198–7209 (2006).
42. P. Ye, J. L. Paredes, G. R. Arce, Y. Wu, C. Chen, and D. W. Prather, "Compressive confocal microscopy," in *IEEE International Conference on Acoustics, Speech and Signal Processing, 2009. ICASSP 2009* (2009), pp. 429–432.

43. V. Studer, J. Bobin, M. Chahid, H. S. Mousavi, E. Candes, and M. Dahan, "Compressive fluorescence microscopy for biological and hyperspectral imaging," *PNAS* **109**, E1679–E1687 (2012).
44. J. H. Shapiro, "Computational ghost imaging," *Phys. Rev. A* **78**, 061802 (2008).
45. G. Scarcelli, V. Berardi, and Y. Shih, "Can Two-Photon Correlation of Chaotic Light Be Considered as Correlation of Intensity Fluctuations?," *Phys. Rev. Lett.* **96**, 063602 (2006).
46. A. Gatti, E. Brambilla, M. Bache, and L. A. Lugiato, "Correlated imaging, quantum and classical," *Phys. Rev. A* **70**, 013802 (2004).
47. B. I. Erkmen and J. H. Shapiro, "Unified theory of ghost imaging with Gaussian-state light," *Phys. Rev. A* **77**, 043809 (2008).
48. G. Brida, M. V. Chekhova, G. A. Fornaro, M. Genovese, E. D. Lopaeva, and I. R. Berchera, "Systematic analysis of signal-to-noise ratio in bipartite ghost imaging with classical and quantum light," *Phys. Rev. A* **83**, 063807 (2011).
49. B. I. Erkmen and J. H. Shapiro, "Signal-to-noise ratio of Gaussian-state ghost imaging," *Phys. Rev. A* **79**, 023833 (2009).
50. M. N. O'Sullivan, K. W. C. Chan, and R. W. Boyd, "Comparison of the signal-to-noise characteristics of quantum versus thermal ghost imaging," *Phys. Rev. A* **82**, 053803 (2010).
51. N. D. Hardy and J. H. Shapiro, "Ghost imaging in reflection: resolution, contrast, and signal-to-noise ratio," *Proceedings of SPIE* **7815**, 78150L–78150L–13 (2010).
52. R. A. Hoebe, C. H. V. Oven, T. W. J. Gadella, P. B. Dhonukshe, C. J. F. V. Noorden, and E. M. M. Manders, "Controlled light-exposure microscopy reduces photobleaching and phototoxicity in fluorescence live-cell imaging," *Nature Biotechnology* **25**, 249–253 (2007).
53. I. M. Vellekoop, E. G. van Putten, A. Lagendijk, and A. P. Mosk, "Demixing light paths inside disordered metamaterials," *Opt. Express* **16**, 67–80 (2008).
54. I. Vellekoop and C. Aegerter, "Scattered light fluorescence microscopy: imaging through turbid layers," *Opt. Lett.* **35**, 1245–1247 (2010).
55. R. Di Leonardo and S. Bianchi, "Hologram transmission through multi-mode optical fibers," *Opt. Express* **19**, 247–254 (2011).
56. T. Čižmár and K. Dholakia, "Shaping the light transmission through a multimode optical fibre: complex transformation analysis and applications in biophotonics," *Opt. Express* **19**, 18871–18884 (2011).

57. J. Aulbach, B. Gjonaj, P. M. Johnson, A. P. Mosk, and A. Lagendijk, "Control of Light Transmission through Opaque Scattering Media in Space and Time," *Phys. Rev. Lett.* **106**, 103901 (2011).
58. O. Katz, E. Small, Y. Bromberg, and Y. Silberberg, "Focusing and compression of ultrashort pulses through scattering media," *Nat Photon* **5**, 372–377 (2011).
59. D. J. McCabe, A. Tajalli, D. R. Austin, P. Bondareff, I. A. Walmsley, S. Gigan, and B. Chatel, "Spatio-temporal focusing of an ultrafast pulse through a multiply scattering medium," *Nat Commun* **2**, 447 (2011).
60. I. M. Vellekoop and A. P. Mosk, "Phase control algorithms for focusing light through turbid media," *Optics Communications* **281**, 3071–3080 (2008).
61. S. Popoff, G. Lerosey, M. Fink, A. C. Boccara, and S. Gigan, "Image transmission through an opaque material," *Nat Commun* **1**, 81 (2010).
62. P. Sen, B. Chen, G. Garg, S. Marschner, M. Horowitz, M. Levoy, and H. Lensch, "Dual Photography," in *SIGGRAPH 2005* (2005), p. 27.
63. A. J. Thompson, C. Paterson, M. A. A. Neil, C. Dunsby, and P. M. W. French, "Adaptive phase compensation for ultracompact laser scanning endomicroscopy," *Opt. Lett.* **36**, 1707–1709 (2011).
64. I. Freund, "Correlation imaging through multiply scattering media," *Physics Letters A* **147**, 502–506 (1990).
65. I. Freund, "Image-reconstruction through multiple-scattering media," *Optics Communications* **86**, 216–227 (1991).
66. I. Freund, "Looking through walls and around corners," *Physica A* **168**, 49–65 (1990).
67. I. Freund, "Time-reversal symmetry and image-reconstruction through multiply-scattering media," *Journal of the Optical Society of America a-Optics Image Science and Vision* **9**, 456–463 (1992).
68. S. H. Simon, A. L. Moustakas, M. Stoytchev, and H. Safar, "Communication in a disordered world," *Physics Today* **54**, 38–43 (2001).
69. G. Lerosey, J. de Rosny, A. Tourin, A. Derode, G. Montaldo, and M. Fink, "Time reversal of electromagnetic waves and telecommunication," *Radio Sci.* **40**, RS6S12 (2005).

70. A. Derode, A. Tourin, J. de Rosny, M. Tanter, S. Yon, and M. Fink, "Taking Advantage of Multiple Scattering to Communicate with Time-Reversal Antennas," *Physical Review Letters* **90**, 014301 (2003).
71. G. Lerosey, J. de Rosny, A. Tourin, A. Derode, G. Montaldo, and M. Fink, "Time Reversal of Electromagnetic Waves," *Physical Review Letters* **92**, 193904 (2004).
72. A. L. Moustakas, H. U. Baranger, L. Balents, A. M. Sengupta, and S. H. Simon, "Communication through a diffusive medium: Coherence and capacity," *Science* **287**, 287–290 (2000).
73. S. E. Skipetrov, *Wireless Communications with Diffuse Waves* (2002).
74. S. E. Skipetrov, "Information transfer through disordered media by diffuse waves," *Phys Rev E Stat Nonlin Soft Matter Phys* **67**, 036621 (2003).
75. M. R. Andrews, P. P. Mitra, and R. deCarvalho, "Tripling the capacity of wireless communications using electromagnetic polarization," *Nature* **409**, 316–318 (2001).
76. T. Kohlgraf-Owens and A. Dogariu, "Spatially resolved scattering polarimeter," *Opt. Lett.* **34**, 1321–1323 (2009).
77. T. W. Kohlgraf-Owens and A. Dogariu, "Transmission matrices of random media: means for spectral polarimetric measurements," *Opt. Lett.* **35**, 2236–2238 (2010).